Research Article

Magnetohydrodynamic mixed convection of TiO_2–Cu/water between the double lid-driven cavity and a central heat source surrounding by a wavy tilted domain of porous medium under local thermal non-equilibrium

M. A. Mansour[1] · M. A. Y. Bakier[1]

Received: 3 August 2022 / Accepted: 15 December 2022
Published online: 09 January 2023

Abstract

The magnetohydrodynamic (MHD) mixed convection of heat and mass transfer is carried out using finite difference method applied inside a tilted porous cavity saturated with a hybrid nanofluid due to the presence of the double-moving lid and the heat sources. In contrast to the earlier research, various effects which are recognized by heat generation in the local thermal non-equilibrium case at the extended Brinkman Darcy model subjected to inclined magnetic field are thoroughly examined numerically. For instance, unusual observations of the cold mass surrounding the heat source emphasize that the maximum fluid temperature highly depends on the forced convection. Additionally, solid-phase temperature acts in accordance to the heat source location while fluid temperature is agitated by the moveable sides which points up the disparity at the thermal energy transportation. However, the transfer of heat and mass at the model requires a specific conduct due to the existence of damping factors. The magnetic field, for example, suppresses the fluid flow. Moreover, the thermal non-equilibrium condition deteriorates the global heat generation.

Article Highlights

- The flow shear at the proposed model is more feasible for the heat and mass transfer than the buoyancy force.
- Local thermal non-equilibrium case creates inaccessible regions that disapprove the harmony in the flow behavior.
- The ratio of natural to forced convection is the most pertinent to the thermal nonequilibrium scenario.

Keywords MHD mixed convection · Porous medium · Hybrid nanofluid · Local non-thermal equilibrium · Wavy sides · Circular heat source · Nusselt number

List of symbols

B_0	Magnetic field strength
C	Concentration
C_p	Specific heat at constant pressure (J kg K^{-1})
Da	Darcy number
g	Acceleration due to gravity (m s^{-2})
Gr	Grashof number, $Gr = \frac{g\beta_f H^4 q_w}{v^2{}_f . k_f}$
H	Length of cavity (m) or reference length
H^*	Inter-phase heat transfer coefficient
Ha	Hartmann number, $B_0 H \sqrt{\sigma_f / \mu_f}$
K	Thermal conductivity (W m^{-1} K^{-1})
k_r	Modified conductivity ratio
N	Normal vector
Nu_m	Average Nusselt Number
Nu_s	Local Nusselt number
P	Dimensionless pressure, $pH/\rho_{nf}\alpha_f^2$

M. A. Y. Bakier, mohameda.yousof@gmail.com | [1]Department of Mathematics, Faculty of Science, Assiut University, Assiut 71515, Egypt.

p	Fluid pressure (Pa)
Pr	Prandtl number, υ_f/α_f
Q	Constant heat flux
Q_0	Heat generation/absorption coefficient
Re	Reynolds number, $U_0 H/\upsilon_f$
Ri	Richardson Number
T	Temperature
U, *V*	Dimensionless velocity components, u/U_0, v/U_0
u, *v*	Velocity components in *x, y* directions (m s^{-1})
X, *Y*	Dimensionless coordinates, *x/H, y/H*
x, *y*	Cartesian coordinates (m)

Greek symbols

ε	Porosity
ρ	Density (kg m^{-3})
φ	Dimensionless concentration
θ	Dimensionless temperature
μ	Dynamic viscosity (N s m^{-2})
σ	Effective electrical conductivity (μS cm^{-1}), S for siemens
ν	Kinematic viscosity (m^2 s^{-1})
Φ	Magnetic field inclination angle
ϕ	Solid volume fraction
α	Thermal diffusivity (m^2 s^{-1}), $k/\rho c_p$
β	Thermal expansion coefficient (K^{-1})

Subscripts

0	Reference
C	Cold
bf	base fluid
h	Hot
hnf	Hybrid nanofluid
m	Average
p	Nanoparticle
s	Solid phase
w	Wall

1 Introduction

Mixed convection with magnetic fields is successfully used in polymers, metallurgy, geothermal energy extraction, and fusion reactors. Due to its properties, it is utilized in a wide range of industries, including mechanical engineering, the petroleum industry, chemical engineering, the medical profession, and other physiological frameworks [1–5]. This idea is especially helpful for applications like magnetic resonance imaging, blood pumping, radiofrequency ablation, cancer tumor treatment, nuclear reactor cooling, magnetic electro-catalysis, metallurgical processes, thermal protection, receiving and transmitting antennas, magnetic electro-catalysis [6–10], etc.

Additionally, obstructions existence at the convection have been compared by Scott et al. [11] to the opening function, where the blockages are like flaps. They split motion into two main categories: bulk density variations and motion pressure gradient, which may both be utilized to explain natural convection flow in multizone enclosures. Partitions should span the ground and roof of a square cavity, according to Chang et al. [12], such that heat transfer reduces as the thickness of the partition climbs. Moreover, Eshaghi et al. [13] have studied the double-diffusive natural convection in an H-shaped cavity with a baffle. They reported that the best Nusselt number and Sherwood number have been grasped. According to Nansteel and Greif [14] and Lin and Bejan [15], impediments between zones tend to keep the boundary layer's thermal equilibrium condition stable, which suggests a general drop in convective heat transmission. As per Sahoo et al. [16], the rectangular blockage at the vertical channel causes a "fluid flow step" that is "backward-facing" and can alter the maximum average temperature. In addition, heat transmission in vertical channels with semi-circular barriers has been studied by Said and Krane [17]. Depending on the Rayleigh number, the obstruction resulted in a drop in the average Nusselt number at a uniform wall temperature (it increases as Ra decreases). In the same context, Seyyedi et al. [18] have investigated heat transfer characteristics as well as entropy generation in a hexagonal enclosure. While, An economic analysis was carried out [19] for heat transfer between two non-similar circular cylinders. However, Dogonchi et al. [20] have proved that the suction process has a dual effect on heat transfer and fluid flow using the Duan-Rach approach.

Shahriari et al. [21] reported their findings in a research on Magnetohydrodynamic natural convection within the angled undulating cavity packed with CuO-water nanofluid. They observed that the magnetic field's inhibitory impact causes the mean Nusselt number and Bejan number to become decreasing functions as the Hartmann number increases, while entropy formation is enhanced. Another illustration is Sheremet et al.'s [22] study of the Magnetohydrodynamic non-driven convection of a nano-fluid in an open porous "high cavity" with a "corner heater". Moreover, Dogonchi et al. [23] reported that "Rayleigh number could overshoot the velocity gradient" for the natural convection at a porous medium saturated between two square cylinders filled with magnetic nanofluids. In addition, Mandal et al. [24] studied the magnetohydrodynamic mixed bioconvection.

On the other hand, the larger amplitude and higher frequency of the moving wall can effectively mix the viscous fluid, according to a significant study by Li et al. [25].

Moreover, Zou et al. [26] concluded that the flow direction should be taken into account to promote convective mixing. To examine the effects of the Lorentz force on the free convection inside the wavy triangular cavity, Shekaramiz et al. [27] carried out a numerical research. They discovered that entropy generation first rises with rising Hartmann numbers before remaining constant.

For instance, in a square cavity containing Cu-water nanofluids, Rashad et al. team 's [28] numerically examined the MHD mixed convection flow. In a porous cavity with a lid with a "Cattaneo-Christov" heat flux pattern by mixed convection, Jakeer et al. [29] numerically investigated the effect of the heated barrier location on the magneto-hybrid nanofluid flow. For MHD natural convection, Sheikholeslami and Sadoughi [30] investigated the "lattice Boltzmann" technique inside a porous cavity that was filled with a nanofluid enclosing that contained 4 square-heaters. In addition, CuO-MWCNT-oil hybrid nanofluid's turbulent flow field, heat transfer, and entropy formation in a trapezoidal container under the influence of a magnetic field were all quantitatively investigated by Aghaei et al. [31] using the finite volume approach. According to their research, the average Nusselt numbers for different Rayleigh numbers and Hartmann numbers decrease with the increased "volume fraction" of nanoparticles. Additionally, the efficiency of heat exchange is dramatically altered by the nanoparticles dispersed, especially those made of metals (Cu, Al_2O_3, ZnO, Ag, and SiO_2) inside the fluid matrix as compared to regular liquid flows (Khanafer et al., Chamkha et al., and Aly et al., [32–35]). Tiwari and Das [36] looked into the supplementary effect for a lid-driven cavity, while Billah et al. [37] looked into the buoyancy-driven force at a slanted triangular compartment. Moreover, The Nusselt number greatly change based on the shape of the used nanoparticles [38].

In accordance with the size, form, and composition of the nanoparticles that are dispersed inside them, nanofluids have different thermal conductivities (Suresh et al. [39]). For instance, metallic particles have a "higher thermal conductivity than non-metallic particles". Nevertheless, as a result of their size, cylindrical nanoparticles function better thermally than spherical nanoparticles ones. Consequently, when the atomic structure of the fluid matrix is precisely treated, significant changes take place. For businesses looking for a product that exhibits excellent stability and superior chemical inertness, Al_2O_3 is the solution. However, this will oftentimes be inadequate for nanofluid applications because they will lose their benefit of heat conductivity. This problem can be handled by adding a few metal particles to an aluminum framework to improve its thermal characteristics. By chemically preparing $CuO–Al_2O_3$ combinations and hydrogen-reducing them, Jeena et al. [40] created the $Cu–Al_2O_3$ nanocomposites. Biswas et al. [41] were able to rise the thermal performance at a tilted porous cavity using $Cu–Al_2O_3$–water nanofluid subjected to the partially active magnetic field. Sung-Tag Oh et al. [42] demonstrated the fabrication of an Al_2O_3–Cu nanocomposite using powder mixtures of fine Al_2O_3 and copper oxide sizes. As an Al_2O_3–Cu/water hybrid nanofluid flowed through a circular tube with a constant heat flux, Suresh et al. [39] assessed the "Nusselt number and friction factor". Davood Toghraie et al. [43] concluded from their experimental studies on $ZnO–TiO_2$/EG hybrid nanofluids that the significant increase in heat transmission occurs either at a warmer temperature proportionate to solid volume fraction or vice versa.

However, it is reported that when carbon nanotubes (CNTs) were attached to the surface of spherical oxide nanoparticles (Huang et al. [44]) then the thermal conductivity was significantly enforced (Han et al. [45]) due to the strong thermal action among the CNTs attached to the alumina/iron oxide particle. On the other hand, nanoencapsulated phase change material has been utilized [46] for free convection in a porous, wavy enclosure. For a better comprehension, Suresh et al. [39] discovered that for a hybrid Al_2O_3–Cu/deionized water nanofluid with a "0.1% volume concentration", the Nusselt number "was 13.56% greater than that of water at *Reynold number* (Re) = 1730". Furthermore, Labib et al. [47] reported that improved heat transmission in mixes of Al_2O_3 nanoparticles in CNT/water nanofluids is enabled by the shear shining features of CNT nanofluids. We contend that because the increment is independent of any discernible chemical change in the research area, qualitative advancement can happen at the heat transfer. The distribution of Nusselt numbers at cavities, on the other hand, is said to follow the geometric pattern of the wall by Arefmanesh et al. [48], which is one of the key purposes of wavy walls at cavities. Engineers can create thermal access points depending on flexible usage at various locations using these models. Additionally, it reduced the development of entropy (Alsabery et al. [49]). Alongside, Das and Mahmud [50] discovered that the heat exchange rate is significantly influenced by the amplitude of the wavy wall and the amount of undulations, particularly in the convective mode (Kumar [51]). A further important aspect is that when the hollow wall is wave shaped, the fluid domain is vulnerable to some disruption, as is the case in storm courses, earthquake systems, and maritime transportation.

Nevertheless, because various mediums have varying temperatures, heat transportation to trace energy dynamics follows a path along a temperature gradient. The viewpoint of thermal equilibrium is used to analyze the above phenomenon. In contrast, the term "local thermal non-equilibrium" (LTNE) is used to describe situations in which there is a "significant seepage velocity, a significant temperature difference between the fluid and solid matrix of a porous medium, or when a heat source exists in either a solid domain or a pure fluid domain within the porous medium" as was stated by Alsabery et al. [52]. Accordingly, when the *heat transmission coefficient* is low, the temperature of the solid phase is lower than the temperature of the fluid phase as a result of Baytaş's [53] application of a heat source to the solid phase. Aside from that, Sheremet et al. [54] show that a lower *interface heat transfer coefficient* implies to decrease in the heat exchange rate, which inhibits the LTNE. In addition, Zargartalebi et al. [55] found that the buoyancy ratio has a negative impact on the heat exchange ratio while positively affecting the Rayleigh number. This finding indicates that the Rayleigh number enhances the thermal equilibrium because the thermal transport via diffusion is greater than that via convection. The system's increasing entropy state, however, causes the buoyancy ratio to induce a non-equilibrium state to rise.

In light of the influence of Buongiorno's concept, Tahmasebi et al. [56] discovered that speeding up the exchange of heat at the interface entails slowing down the interchange of the micro liquid phase. Regarding Brownian motion, this model. On the basis of our knowledge, Brownian motion prevents heat exchange at the contact. However, Nield et al. [57] found that the local Nusselt number is poorly dependent on the Darcy number or the fluid–solid heat exchange parameter and relies entirely on the Peclet number and the solid/fluid conductivity. This could be due the advection/diffusion regimes are so effective since the velocity profile overtakes heat transfer in boundary layer flows. Nonetheless, we may conclude that there is a connection between the Darcy number and the heat exchange parameter in that scenario to understand why the heat exchange is ineffective. The reliability of the local thermal equilibrium for all porous media when the conduction mode is predominate has been shown by Kim and Jang [58].

Furthermore, when the interstitial heat transfer coefficient is proportional to $Re^{exponent>1}$ (such as sintered metals and cellular ceramics) and the convection mode is dominant, the local thermal equilibrium is applicable. For the purpose of choosing an appropriate analytical interpretation, Amiri et al. [59] made the supposition that the constant heat flux at boundaries is satisfied when either heat propagation is based on temperature gradients (effective conductivities) or each phase receives the same amount of the flux at the interface. In addition, Mahmoudi and Karimi [60] have shown that the Nusselt number for the first method is higher than the other one for the second. The Darcy number was negatively associated with the thickness of the local thermal non-equilibrium porous zone, which they were able to measure. Aside from that, Izadi et al. [61] have observed that the thermal nonequilibrium case deteriorates as the thermal conductivity ratio and heat transfer parameter increase. Moreover, the reduction in the thermal resistance [76] of fluid phase can enhance the heat transmission rate due to the increase in the thermal conductivity ratio. In addition, permeability influences the Nu number (the dimensionless quantity) of both solid/fluid phases due to nanoparticles rotating around the center of gravity. Sivasankaran et al. [62] have found that exchange speed of thermal energy is enhanced by increasing values of the modified conductivity ratio and the porosity of the media. Entirely, Tahmasebi et al. [63] have found that the average Nu is supported by Rayleigh number, Darcy number, and thermal conductivity ratios at solid and fluid phases. Furthermore, the convection interaction regime at pores increases the Nu for the solid phase whereas decreases it for the nano-fluid.

Regarding the running study, the control parameters of the model encompasses various heat and mass dynamics have been analyzed numerically in line with the MHD mixed convection around a central circular heat source and the other cold wavy boundaries. The manuscript is organized as following; first section is the introduction where we shed light on the different styles of heat transfer mechanisms due to fluid flow within miscellaneous media under different conditions. In the second section, the mathematical formulation for the problem is designated. Then the fundamentals of the numerical investigation are demonstrated in the third section. Therefore, at section four, the results are displayed in the form of the contours of the temperature and fluid flow which disclose the active regions within the cavity while the Nusselt number profiles monitor the heat flux behavior at the boundaries. Ultimately, the fifth section sum up the findings of the proposed work.

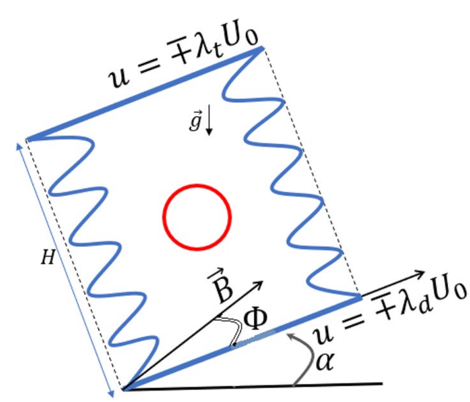

Fig. 1 Schematic diagram of the model

2 Mathematical modeling

Figure 1 shows the preliminary geometry of an undulating inclined cavity. The involved wavy cavity is filled by porous media and hybrid nanofluids. The flow of porous medium is subjected to the extension of Darcy's law using Dupuit-Forchheimer relationship. The right and left side wavy-walls are cold (T_c), the bottom and top sides are adiabatic. Moreover, the fluid domain is inclined with angle α and the magnetic field has an inclination angle Φ. The hybrid nanofluid convection is not in a local thermodynamic equilibrium condition. The normal direction and constant value are considered for the gravity acceleration. Dirichlet type applied on all boundaries (no-slip condition). According to the previously specified hypotheses, continuity, momentum, concentration, and energy equations are formulated for hybrid nanofluids, incompressible, laminar, and single-phase flows in steady-state as follows [64, 65]:

$$\frac{\partial u}{\partial x}+\frac{\partial v}{\partial y}=0 \tag{1}$$

$$\frac{1}{\varepsilon^2}\left(u\frac{\partial u}{\partial x}+v\frac{\partial u}{\partial y}\right)=-\frac{1}{\rho_{hnf}}\frac{\partial p}{\partial x}+\frac{1}{\varepsilon}.\frac{\mu_{hnf}}{\rho_{hnf}}.\nabla^2 u-\frac{\mu_{hnf}}{\rho_{hnf}}.\frac{u}{K}+\frac{(\rho\beta)_{hnf}}{\rho_{hnf}}g(T_f-T_c)\sin\alpha+\frac{(\rho\beta^*)_{hnf}}{\rho_{hnf}}g(C-C_c)\sin\alpha+\frac{\sigma_{hnf}B_0^2}{\rho_{hnf}}\left(v\sin\Phi\cos\Phi-u\sin^2\Phi\right) \tag{2}$$

$$\frac{1}{\varepsilon^2}\left(u\frac{\partial v}{\partial x}+v\frac{\partial v}{\partial y}\right)=-\frac{1}{\rho_{hnf}}\frac{\partial p}{\partial y}+\frac{1}{\varepsilon}.\frac{\mu_{hnf}}{\rho_{hnf}}.\nabla^2 v-\frac{\mu_{hnf}}{\rho_{hnf}}.\frac{v}{K}+\frac{(\rho\beta)_{hnf}}{\rho_{hnf}}g(T_f-T_c)\cos\alpha+\frac{(\rho\beta^*)_{hnf}}{\rho_{hnf}}g(C-C_c)\cos\alpha+\frac{\sigma_{hnf}B_0^2}{\rho_{hnf}}\left(u\sin\Phi\cos\Phi-v\cos^2\Phi\right) \tag{3}$$

$$\frac{1}{\varepsilon}\left(u\frac{\partial T_f}{\partial x}+v\frac{\partial T_f}{\partial y}\right)=\alpha_{eff.hnf}.\nabla^2 T_f+\frac{h_{hnfs}(T_s-T_f)}{\varepsilon(\rho c_p)_{hnf}}+\frac{Q_0}{\varepsilon(\rho c_p)_{hnf}} \tag{4}$$

$$0=(1-\varepsilon)[k_s+\frac{16\sigma^* T_c^3}{3k^*}].\nabla^2 T_s+h_{nfs}(T_f-T_s)+(1-\varepsilon)Q_0 \tag{5}$$

$$u\frac{\partial C}{\partial x}+v\frac{\partial C}{\partial y}=D_B.\nabla^2 C \tag{6}$$

The boundary conditions imposed on the flow field are taken as:

On the left wall

$$u=v=0, T_f=T_s=T_c, C=C_c, x=AH\left[1-cos(2\pi\lambda y/H)\right], 0\le y\le H \tag{7.1}$$

On the right wall

$$u=v=0, T_f=T_s=T_c, C=C_c, x=H-AH\left[1-cos(2\pi\lambda y/H)\right], 0\le y\le H \tag{7.2}$$

On the top wall

$$u=\pm\lambda_t U_0, v=0, T_f=T_s=T_c, C=C_c, 0\le x\le H \tag{7.3}$$

On the bottom wall

$$u=\pm\lambda_d U_0, v=n=0, T_f=T_s=T_c, C=C_c, 0\le x\le H \tag{7.4}$$

On the inner circular cavity

$$T_f=T_s=T_h \tag{8}$$

where u and v are the velocity components, T is temperature, s-index refers to solid phase, f-index refers to fluid phase, C stands for the concentration of nanoparticles, ρ_{hnf} is the density of the hybrid nanofluid, v_{hnf} is kinematic viscosity. g is a gravity, p is a pressure, μ_{hnf} is a dynamic viscosity, $\beta^*=(-1/\rho)(d\rho/dC)_{T,p}$, the buoyancy rate due to nanoparticle concentration currents, and Q_0 is the heat generation.

2.1 Dimensionless forms of equations

Presenting the next non-dimensional variables (Eq. 9) into Eqs. (1)–(7) yields the dimensionless equations (Eqs. 10–15):

$$X,Y=\frac{x,y}{H}, U,V=\frac{u,v}{U_0}, P=\frac{p}{\rho_{nf}U_0^2}, \theta_f=\frac{(T_f-T_c)}{(T_h-T_c)}, \theta_s=\frac{(T_s-T_c)}{(T_s-T_c)}, \varphi=\frac{(C-C_c)}{(C_h-C_c)}, Ri=\frac{Gr}{Re^2}, Re=\frac{U_0H}{v_f} \tag{9}$$

$$\frac{\partial U}{\partial X}+\frac{\partial V}{\partial Y}=0 \tag{10}$$

$$\begin{aligned}\frac{1}{\varepsilon^2}\left(U\frac{\partial U}{\partial X}+V\frac{\partial U}{\partial Y}\right)=&-\frac{\partial P}{\partial X}+\frac{1}{\varepsilon\cdot Re}\cdot\left(\frac{\rho_f}{\rho_{hnf}}\right)\left(\frac{\mu_{hnf}}{\mu_f}\right)\cdot\nabla^2U\\&-\frac{1}{Da\cdot Re}\cdot\left(\frac{\rho_f}{\rho_{hnf}}\right)\left(\frac{\mu_{hnf}}{\mu_f}\right)\cdot U\\&+Ri\cdot\frac{(\rho\beta)_{hnf}}{\rho_{hnf}\cdot\beta_f}\sin\alpha\cdot\theta_f+Gr_c\cdot\sin\alpha\cdot\phi\\&+\left(\frac{\rho_f}{\rho_{hnf}}\right)\left(\frac{\sigma_{hnf}}{\sigma_f}\right)\cdot\frac{Ha^2}{Re}\left(V\sin\Phi\cos\Phi-U\sin^2\Phi\right)\end{aligned} \tag{11}$$

$$\begin{aligned}\frac{1}{\varepsilon^2}\left(U\frac{\partial V}{\partial X}+V\frac{\partial V}{\partial Y}\right)=&-\frac{\partial P}{\partial Y}+\frac{1}{\varepsilon\cdot Re}\cdot\left(\frac{\rho_f}{\rho_{hnf}}\right)\left(\frac{\mu_{hnf}}{\mu_f}\right)\cdot\nabla^2V\\&-\frac{1}{Da\cdot Re}\cdot\left(\frac{\rho_f}{\rho_{hnf}}\right)\left(\frac{\mu_{hnf}}{\mu_f}\right)\cdot V\\&+Ri\cdot\frac{(\rho\beta)_{hnf}}{\rho_{hnf}\cdot\beta_f}\cos\alpha\cdot\theta_f+Gr_c\cdot\cos\alpha\cdot\phi\\&+\left(\frac{\rho_f}{\rho_{hnf}}\right)\left(\frac{\sigma_{hnf}}{\sigma_f}\right)\frac{Ha^2}{Re}\left(U\sin\Phi\cos\Phi-V\cos^2\Phi\right)\end{aligned} \tag{12}$$

$$\begin{aligned}\frac{1}{\varepsilon}\left(U\frac{\partial\theta_f}{\partial X}+V\frac{\partial\theta_f}{\partial Y}\right)=&\left(\frac{1}{RePr}\right)\frac{\alpha_{eff.hnf}}{\alpha_f}\cdot\nabla^2\theta_f+\frac{1}{\varepsilon\cdot RePr}\frac{(\rho c_p)_f}{(\rho c_p)_{hnf}}\\&\cdot H^*(\theta_s-\theta_f)+\frac{1}{\varepsilon\cdot RePr}\frac{(\rho c_p)_f}{(\rho c_p)_{hnf}}\cdot Q\end{aligned} \tag{13}$$

$$0=\nabla^2\theta_s+K_r.H^*(\theta_f-\theta_s)+k_{fs}.Q \tag{14}$$

$$U\frac{\partial\varphi}{\partial X}+V\frac{\partial\varphi}{\partial Y}=\frac{1}{Re.Sc}\left(\frac{\partial^2\varphi}{\partial X^2}+\frac{\partial^2\varphi}{\partial Y^2}\right) \tag{15}$$

where $Pr=\frac{\nu_f}{\alpha_f}, Re=\frac{U_0H}{\nu_f}, Gr=\frac{g\beta_fH^3\Delta T}{\nu^2{}_f}, Ha=B_0H\sqrt{\frac{\sigma_f}{\mu_f}}$, $Da=\frac{K}{H^2}, R_d=\frac{16\sigma^*T_c^3}{3k^*k_s}$, the inter-phase heat transfer coefficient;

$$H^*=h_{nfs}.\frac{H^2}{k_f}, Q=Q_0.\frac{H^2}{k_f}, k_{fs}=\frac{k_f}{k_s}, K_r=\frac{k_f}{(1-\varepsilon)k_s}, \tag{16}$$

And the corresponding dimensionless boundary @@ conditions are;

On the left wall:

$$U=V=0,\theta_f=\theta_s=\varphi=0, X=A[1-cos(2\pi\lambda Y)], 0\le Y\le 1 \tag{17.1}$$

On the right wall:

$$U=V=0,\theta_f=\theta_s=\varphi=0, X=1-A[1-cos(2\pi\lambda Y)], 0\le Y\le 1 \tag{17.2}$$

On the top wall

$$U=\pm\lambda_t, V=0,\theta_f=\theta_s=0,\varphi=0, 0\le X\le 1, \tag{17.3}$$

On the bottom wall:

$$U=\pm\lambda_d, V=0,\theta_f=\theta_s=0,\varphi=0, 0\le X\le 1 \tag{17.4}$$

On the inner circular:

$$\theta_f=\theta_s=1 \tag{18}$$

The local Nusselt number of the fluid can be formulated as:

$$Nu_{fs(left,right)}=-\frac{k_{hnf}}{k_f}\left(\frac{\partial\theta_f}{\partial X}\right)_{left,right}, Nu_{fs(Y=0,1)}=-\frac{k_{hnf}}{k_f}\left(\frac{\partial\theta_f}{\partial Y}\right)_{Y=0,1} \tag{19}$$

The local Nusselt number of the solid can be written as:

$$\begin{aligned}Nu_{ss(left,right)}&=-\frac{k_{hnf}}{k_f}(1+R_d)\left(\frac{\partial\theta_s}{\partial X}\right)_{left,right},\\Nu_{ss(Y=0,1)}&=-\frac{k_{hnf}}{k_f}(1+R_d)\left(\frac{\partial\theta_s}{\partial Y}\right)_{Y=0,1}\end{aligned} \tag{20}$$

The average Nusselt number of the fluid and solid are

$$Nu_{mf}=\int_0^H Nu_{fs}dX, Nu_{ms}=\int_0^H Nu_{ss}dX \tag{21}$$

in the above Eq. (13) $\alpha_{eff,hnf}$ is defined as

$$\alpha_{eff,hnf} = \frac{k_{eff,hnf}}{\left(\rho c_p\right)_{hnf}} \tag{22}$$

where

$$k_{eff,hnf} = \varepsilon k_{hnf} + (1-\varepsilon)k_s \tag{23}$$

2.2 Thermophysical properties of nanofluid and hybrid nanofluid

While some research has looked at determining the thermophysical properties of nanoparticles (Table 1), classical models do not necessarily apply to nanofluids. Experimental results facilitate the selection of an appropriate model for a particular property. Defining the effective properties of TiO_2/water nanofluids and TiO_2–Cu/water hybrid nanofluids (Table 1), respectively, are as follows:

$$\rho_{nf} = (1-\phi)\rho_{bf} + \phi\rho_p \tag{24}$$

which determine density of nanofluid, the density of hybrid nanofluid is specified as [66]:

$$\rho_{hnf} = \phi_{TiO_2}\rho_{TiO_2} + \phi_{Cu}\rho_{Cu} + (1-\phi)\rho_{bf} \tag{25}$$

where ϕ is the overall volume concentration of two different types of nanoparticles dispersed in hybrid nanofluid and is calculated as; $\phi = \phi_{TiO_2} + \phi_{Cu}$, and the heat capacitance of the nanofluid given is as,

$$(\rho C_p)_{nf} = \phi(\rho C_p)_p + (1-\phi)(\rho C_p)_{bf} \tag{26}$$

Table 1 Thermophysical properties of water, Copper, and Titanium [69–71]

Property	Water	Copper (Cu)	TiO_2
ρ [kg/m^3]	997.1	8933	4250
C_p [J/kg]	4179	385	686.2
k [W/m K]	0.613	401	8.9538
β [K^{-1}]	21×10^{-5}	1.67×10^{-5}	0.9×10^{-5}
σ [μS/cm]	0.05	5.96×10^{-7}	2.38×10^{6}

where β_{bf} and β_p are the coefficients of thermal expansion of the fluid and of thesolid fractions respectively.

Hence, for hybrid nanofluid, thermal expansion can be defined as follows:

$$(\rho\beta)_{hnf} = \phi_{TiO_2}(\rho\beta)_{TiO_2} + \phi_{Cu}(\rho\beta)_{Cu} + (1-\phi)(\rho\beta)_{bf} \tag{29}$$

Thermal diffusivity,α_{nf} of the nanofluid isdefined as:

$$\alpha_{nf} = \frac{k_{nf}}{(\rho c_p)_{nf}} \tag{30}$$

k_{nf} is the thermal conductivity of the nanofluid which for spherical nanoparticles, according to the Maxwell–Garnetts model [67], is:

$$\frac{k_{nf}}{k_{bf}} = \frac{(k_p + 2k_{bf}) - 2\phi(k_{bf} - k_p)}{(k_p + 2k_{bf}) + \phi(k_{bf} - k_p)}, \tag{31}$$

Thus, thermal diffusivity, α_{hnf} of the hybrid nanofluid can be defined as;

$$\alpha_{hnf} = \frac{k_{hnf}}{(\rho C_p)_{hnf}}, \tag{32}$$

If the thermal conductivity of hybrid nanofluid is defined according to Maxwell model,

$$\frac{k_{hnf}}{k_{bf}} = \left(\frac{\left(\phi_{TiO_2}k_{TiO_2} + \phi_{Cu}k_{Cu}\right)}{\phi} + 2k_{bf} + 2\left(\phi_{TiO_2}k_{TiO_2} + \phi_{Cu}k_{Cu}\right) - 2\phi k_{bf}\right) \times \left(\frac{\left(\phi_{TiO_2}k_{TiO_2} + \phi_{Cu}k_{Cu}\right)}{\phi} + 2k_{bf} - \left(\phi_{TiO_2}k_{TiO_2} + \phi_{Cu}k_{Cu}\right) + \phi k_{bf}\right)^{-1} \tag{33}$$

According to (6), heat capacity of hybrid nanofluid can be determined as follows:

$$(\rho C_p)_{hnf} = \phi_{TiO_2}(\rho C_p)_{TiO_2} + \phi_{Cu}(\rho C_p)_{Cu} + (1-\phi)(\rho C_p)_{bf} \tag{27}$$

The thermal expansion coefficient of the nanofluid can be determined by:

$$(\rho\beta)_{nf} = \phi(\rho\beta)_p + (1-\phi)(\rho\beta)_{bf} \tag{28}$$

The effective dynamic viscosity of the nanofluid based on the Brinkman model [68] is given by

$$\mu_{nf} = \frac{\mu_{bf}}{(1-\phi)^{2.5}} \tag{34}$$

where μ_{bf} is the viscosity of the fluid fraction, then the effective dynamic viscosity of the hybrid nanofluid is;

$$\mu_{hnf} = \frac{\mu_{bf}}{\left(1 - \left(\phi_{TiO_2} + \phi_{Cu}\right)\right)^{2.5}}, \quad (35)$$

and the effective electrical conductivity of nanofluid was presented by Maxwell as

$$\frac{\sigma_{nf}}{\sigma_{bf}} = 1 + \frac{3\left(\frac{\sigma_p}{\sigma_{bf}} - 1\right)\phi}{\left(\frac{\sigma_p}{\sigma_{bf}} + 2\right) - \left(\frac{\sigma_p}{\sigma_{bf}} - 1\right)\phi} \quad (36)$$

and the effective electrical conductivity of hybrid nanofluid is;

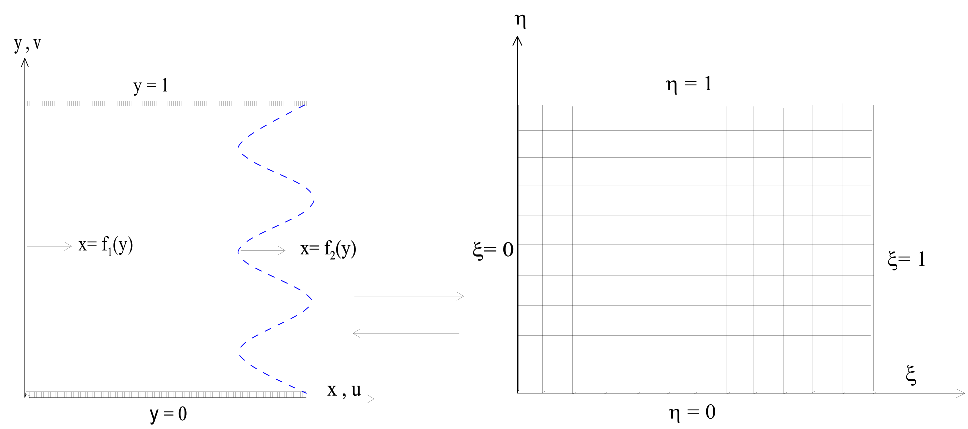

(a) Physical model. **(b)** Computational model.

Fig. 2 Mapping between physical and computational models

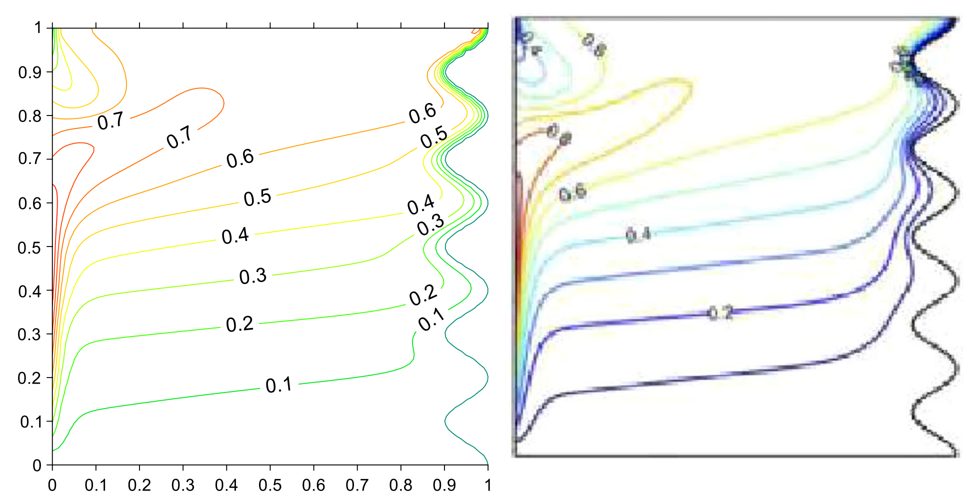

Fig. 3 Comparison between the present results (right) and those obtained by Cheong et al. [74] (left)

Table 2 Comparisons of the horizontal velocity with those of Khanafer and Chamkha [75] at Gr = 100 and Pr = 0.71, $\phi = 0\%$.

Re	Minimum velocity U_{Min}			Maximum velocity U_{Max}		
	Khanafer and Chamkha [75]	Present	Error (%)	Khanafer and Chamkha [75]	Present	Error (%)
100	−0.2122	0.2035	4.99	1.000	1.000	0
400	−0.3099	−0.3212	3.65	1.000	1.000	0

$$\frac{\sigma_{hnf}}{\sigma_{bf}} = 1 + \frac{3\left(\frac{\left(\phi_{TiO_2}\sigma_{TiO_2}+\phi_{Cu}\sigma_{Cu}\right)}{\sigma_{bf}} - \left(\phi_{TiO_2} + \phi_{Cu}\right)\right)}{\left(\frac{\left(\phi_{TiO_2}\sigma_{TiO_2}+\phi_{Cu}\sigma_{Cu}\right)}{\phi\sigma_{bf}} + 2\right) - \left(\frac{\left(\phi_{TiO_2}\sigma_{TiO_2}+\phi_{Cu}\sigma_{Cu}\right)}{\sigma_{bf}} - \left(\phi_{TiO_2} + \phi_{Cu}\right)\right)} \tag{37}$$

3 Numerical method and validation

A grid transformation is accomplished to perform the numerical contributions at an appropriate computational domain which accelerates the convergence of the approximated solutions and averts the numerical errors yielded sometimes from the accumulation of the digital truncations during the improvement of numerical iterations. The variables domain needs to abstain from the geometrical complexity of wavy boundaries, stagnation points, and critical points which often cause disturbances in the approximation solution. This issue could be more realistic from the physical domain view but it sacrifices the stability of the solution environment. Therefore, such an approved computational domain is used with the finite volume method presented in [72, 73] which is extended here to the non-orthogonal grids. This technique starts with definitions of the new coordinates (ξ, η) as following:

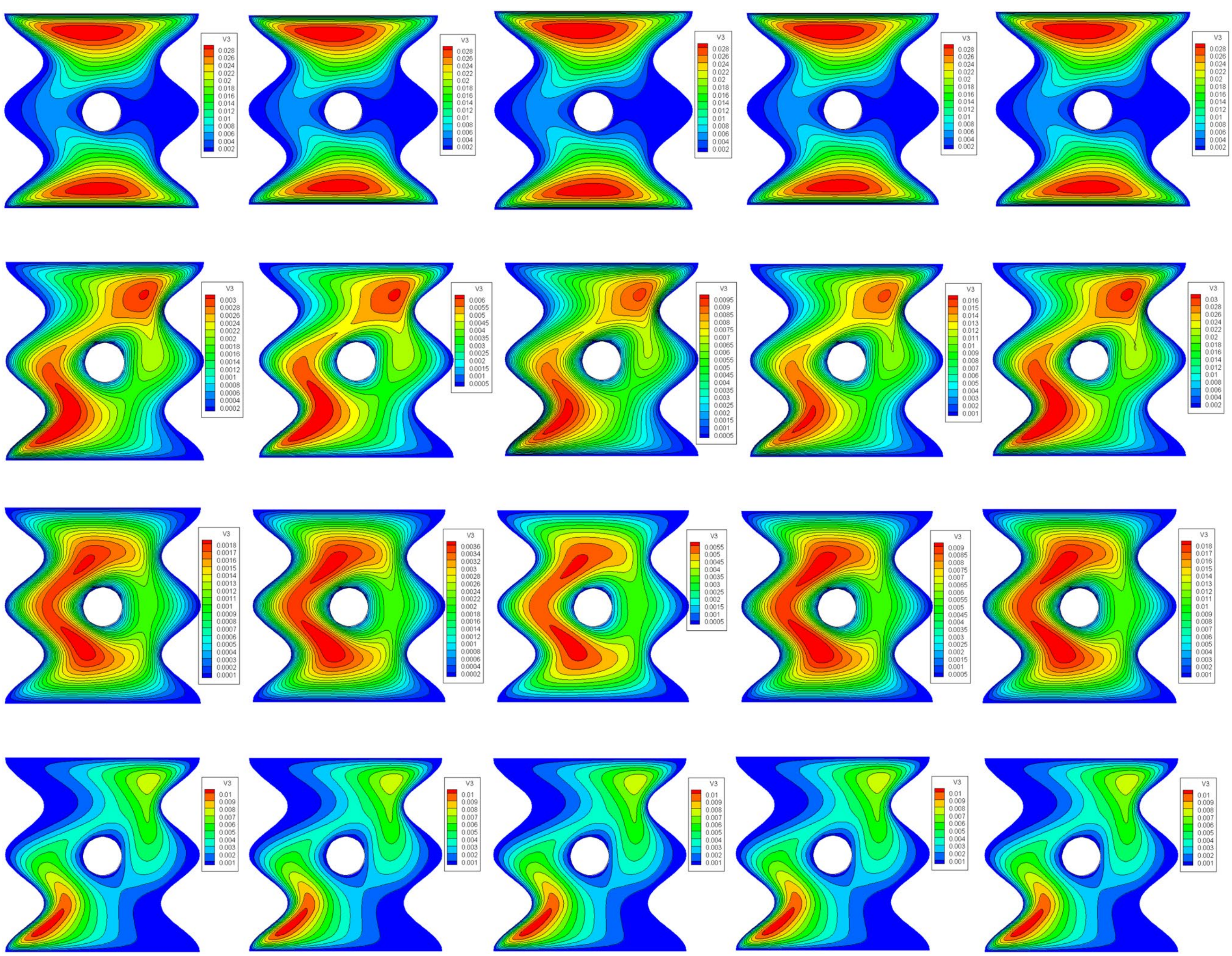

Fig. 4 Effect of heat generation variation (Q = {0.1,0.2,0.3,0.4,0.5, 1} from left to right) on contours of streamlines (1st row), isotherms of fluid phase (2nd row), isotherms of solid phase (3rd row), isoconcentrations (4th row), for TiO_2–Cu/water hybrid nanofluid at the moderate values; $Ha = 10$, $Da = 10^{-3}$, $Ri = 1$, $Gr_c = 1$, $H^* = 10$, $R_d = 0.5$, $\varepsilon = 0.5$, $\gamma = 0.5$, $\Phi = \pi/3$, $\phi_{Cu} = \phi_{TiO2} = \phi/2$, $\phi = 0.05$

$$X_1 = A(1 - \cos(2\pi\lambda Y)),\ X_2 = 1 - A(1 - \cos(2\pi\lambda Y)),\ \xi = \frac{X - X_1}{X_2 - X_1},\quad \eta = Y \tag{38}$$

Using Eq. (38), the irregular physical model is mapping to a rectangular computational model as it is shown in Fig. 2. The resulting transformed system is treated using the finite volume method. Here, the advection terms are evaluated using "the second upwind scheme", whilst the Laplace operators are handled using the central difference methods. Iteratively utilizing ADI (alternating direction implicit), the resultant algebraic structure is solved. This study's convergence criteria were selected to be systematic. Additionally, the size of the grid is discovered to be appropriate for all computations after doing several grid tests. Additionally, Fig. 3 compares the outcomes of the current simulation to those attained by Cheong et al. [74] in certain instances ($\phi=\varphi=Ha=Q=0$). It is discovered that the outcomes are in good accordance with one another. Furthermore, another comparison test is performed with the results of Khanafer and Chamkha [75] where the mixed convection due to the moving of the upper wall of a square enclosure has been examined. Table 2 shows an excellent agreement between the results are obtained.

4 Results and discussion

In this section, the obtained results are presented step-by-step in terms of key parameters such as the heat generation parameter (Q) is varied from 0.1 to 1, the effects of Hartmann number (*Ha*) is varied from 0 to 150, the

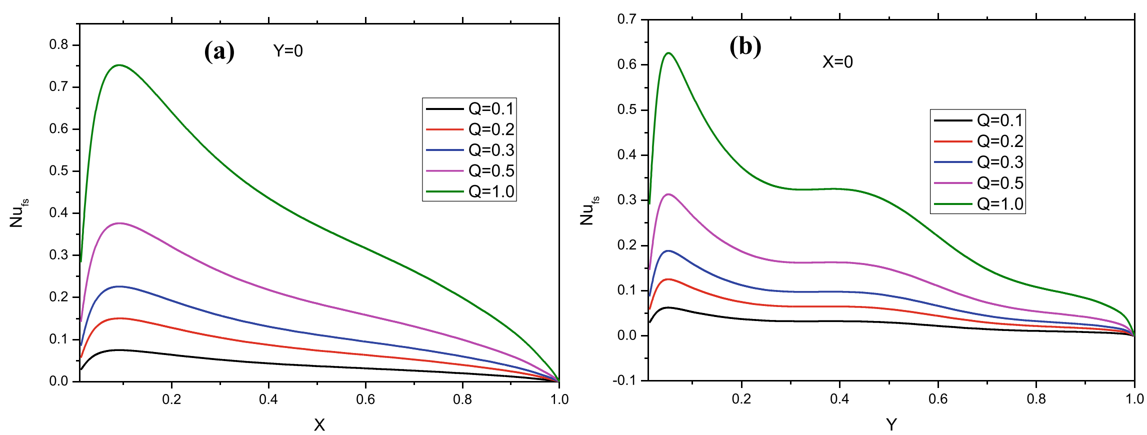

Fig. 5 Heat generation heat transfer parameter profiles of the local Nusselt number of fluid phase for TiO_2–Cu/water Hybrid Nanofluid at $Ha=10, Da=10^{-3}, Ri=1, Gr_c=1, H^*=10, R_d=0.5, \varepsilon=0.5, \gamma=0.5, \Phi=\pi/3, \lambda=, \alpha=, \phi_{Cu}=\phi_{TiO2}=\phi/2, \phi=0.05$

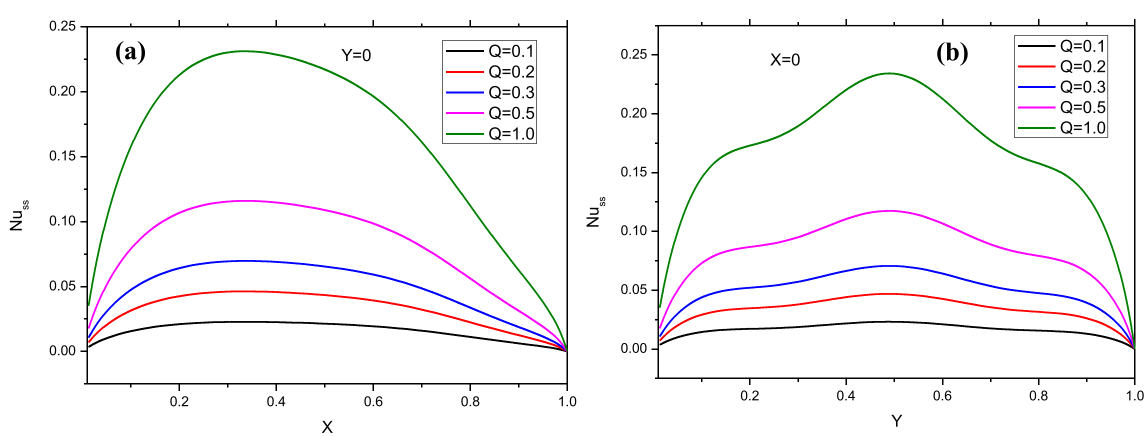

Fig. 6 Heat generation heat transfer parameter profiles of the local Nusselt number of solid phase for TiO_2–Cu/water Hybrid Nanofluid at $Ha=10, Da=10^{-3}, Ri=1, Gr_c=1, H^*=10, R_d=0.5, \varepsilon=0.5, \gamma=0.5, \Phi=\pi/3, \lambda=, \alpha=, \phi_{Cu}=\phi_{TiO2}=\phi/2, \phi=0.05$

radiation parameter 0–5, the porosity parameter (ε) varied as 0.4 to 0.9, the inter-phase heat transfer coefficient (H^*) is varied from 0.005 to 50, the Darcy number (Da) is varied from 10^{-1} to 10^{-5}, Prandtl number $Pr=6.2$, and the nanoparticle volume fraction (ϕ) is varied from 0.01 to 0.05. The obtained results have been illustrated using streamlines, isotherms of fluid phase, isotherms of solid phase, isoconcentrations and Local and average Nusselt and Sherword numbers. Except for the variations in the respective figures, these values are considered to be fixed on the entire computation; $Ha=10$, $\phi_{Cu}=\phi_{TiO2}=\phi/2$, $\phi=0.05$, $Q=1$, $\lambda=2$, $\alpha=\Phi=\pi/3$, $Da=10^{-3}$, $k_r=l$, $\lambda_d=\lambda_t=1$, and $\gamma=0.5$.

It is important to glance on the prominent terms at the governing equations. For example for momentum conservation equations, the surface forces are represented by the pressure components at the porous medium, while the body forces come from gravitational term which the linear combination of both heat and nanoparticles concentration and the magnetic field. The term $H^*(\theta_s-\theta_f)$ in energy equation points to the internal heat exchange between the solid and fluid phases which characterizes the non-thermal equilibrium at porous medium.

For streamlines as in Fig. 4, there are two vortices of the utmost stream function that are concentrated adjacent to the mobile surfaces (top and bottom). The unnormal issue is the stagnant fluid around the heat source which means that the forced convection dominates more regions than the natural convection. It could be back to the value of Richardson number where "Ri (→ 1)" in this study which is relatively small. The effect of heat generation parameter "Q" is weak due to the non-thermal equilibrium. For the fluid isotherms, two vortices are established near to those of streamlines. Still the amazing event is the cold fluid around the heat source region meaning that the supremum fluid temperature is created basically from forced convection. The solid isotherms are different than fluid isotherms at the location. The isotherms are two adjoining vortices and their centers (maximum solid temperature values) are away from those of streamlines because the solid isotherms approaches to the heat source. The two vortices are united at the left half may be due to the numerical calculations or the effect of the cavity inclination angle. The two solid vortices appeal to make a circle around the heat source. For the interpretation; the non-thermal equilibrium enhances the inconsistency between the fluid and solid isotherms distributions. We can see that fluid temperature is greatly affected by the movable sides while the solid temperature is influenced in the heat source position. the mutual effect between solid and fluid phase could not be neglected but it doesn't represents the basic factor of heat transmission here. Moreover, the iso-concentrations contours are concentrated at the bottom-left corner due to the effect of inclination angle "α".

The fluid Nusselt number along the bottom side (Fig. 5) scores nonzero values at the origin point of the cavity which is the conjunction point of movable bottom side and wavy left side. Besides, Nusselt number completely vanishes when arrives the right side so the left side is so active region while the right corner is semi isolated region at the cavity may be due to the effect of the inclination angle. Normally, As "Q" increases the Nusselt number increases (Fig. 6). On the other hand, the solid Nusselt number along the bottom side is represented by a curve of the second order which is symmetric around the heat source location. Consequently, this represents an evidence of the robust dependency between the heat source position and the heat transfer at the solid phase which has been mentioned above at the contours discussion. In addition, the average Nusselt number (Fig. 7) for the fluid phase is larger (~ 100%) than that of the solid phase, which reflex the strong fluid response to the Q parameter more than the solid phase.

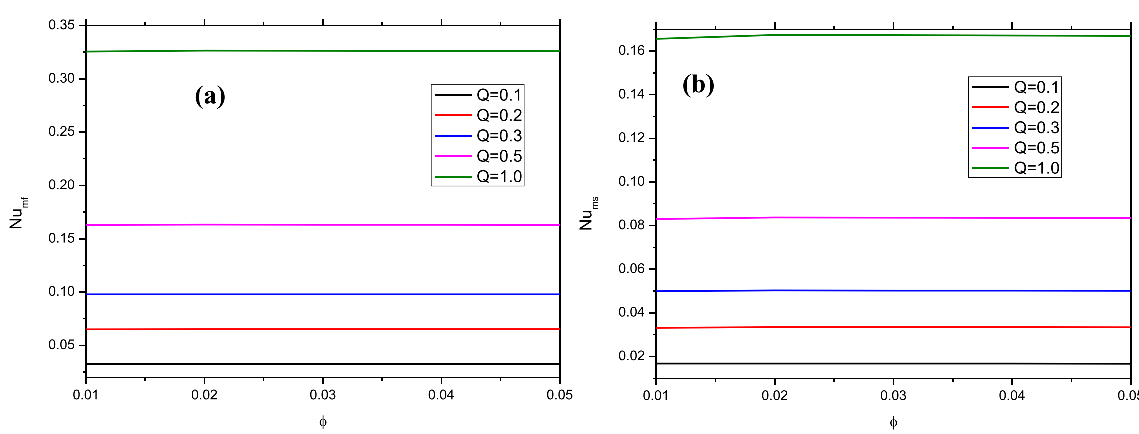

Fig. 7 Heat generation heat transfer parameter profiles of the average Nusselt number of fluid phase (top) and solid phase (bottom) for TiO_2–Cu/water Hybrid Nanofluid at $Ha=10$, $Da=10^{-3}$, $Ri=1$, $Gr_c=1$, $H^*=10$, $R_d=0.5$, $\varepsilon=0.5$, $\gamma=0.5$, $\Phi=\pi/3$, $\lambda=$, $\alpha=$, $\phi_{Cu}=\phi_{TiO2}=\phi/2$, $\phi=0.05$

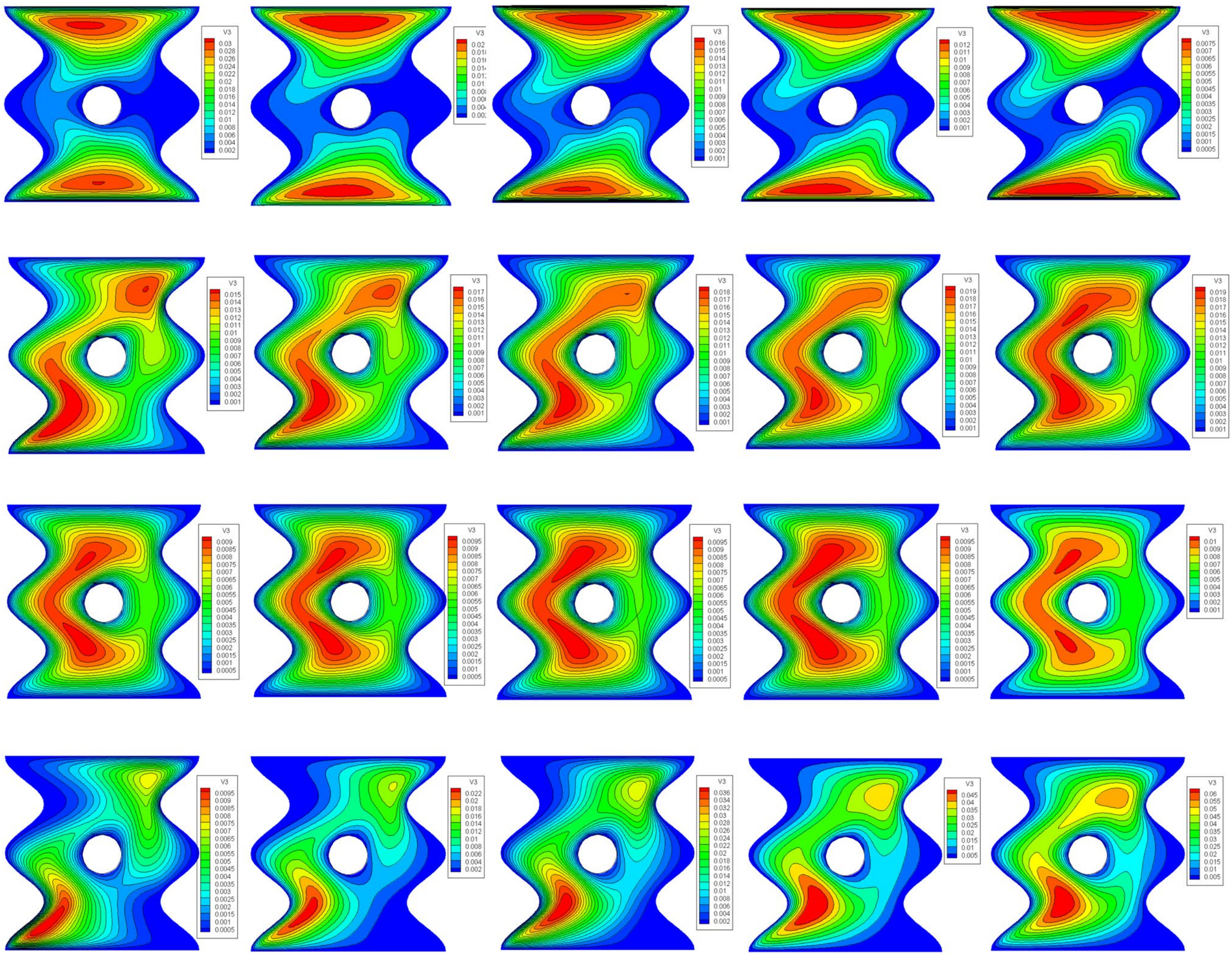

Fig. 8 Effect of Hartmann number variation (Ha = {0, 50, 75, 100, 150}from left to right) on contours of streamlines (1st row), isotherms of fluid phase (2nd row), isotherms of solid phase (3rd row), isoconcentrations (4th row), for TiO_2–Cu/water hybrid nanofluid at the moderate values; $Q = 1$, $Da = 10^{-3}$, $Ri = 1$, $Gr_c = 1$, $H^* = 10$, $R_d = 0.5$, $\varepsilon = 0.5$, $\gamma = 0.5$, $\Phi = \pi/3$, $\lambda =$, $\alpha =$, $\phi_{Cu} = \phi_{TiO2} = \phi/2$, $\phi = 0.05$

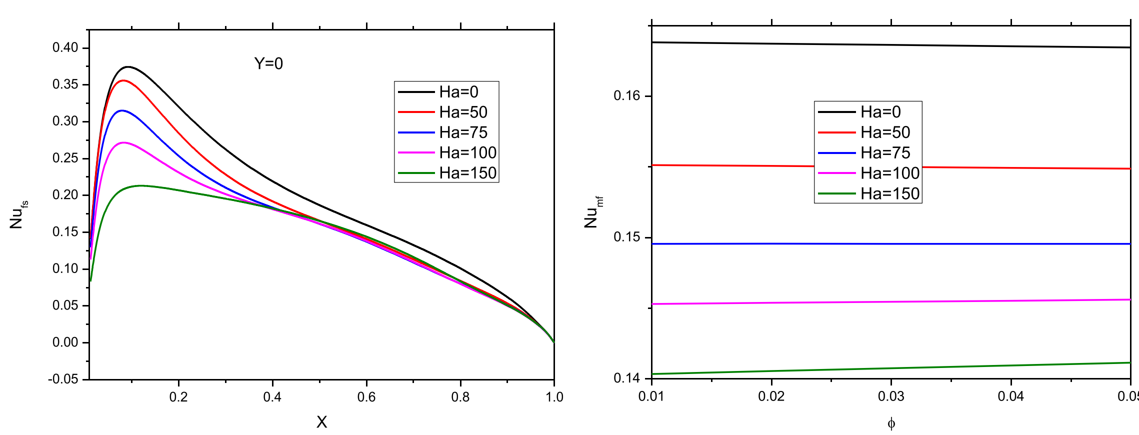

Fig. 9 Hartmann number for heat transfer profiles of the local Nusselt number of fluid phase (left) and average values (right) for TiO_2–Cu/water Hybrid Nanofluid at $Q = 1$, $Da = 10^{-3}$, $Ri = 1$, $Gr_c = 1$, $H^* = 10$, $R_d = 0.5$, $\varepsilon = 0.5$, $\gamma = 0.5$, $\Phi = \pi/3$, $\lambda =$, $\alpha =$, $\phi_{Cu} = \phi_{TiO2} = \phi/2$, $\phi = 0.05$

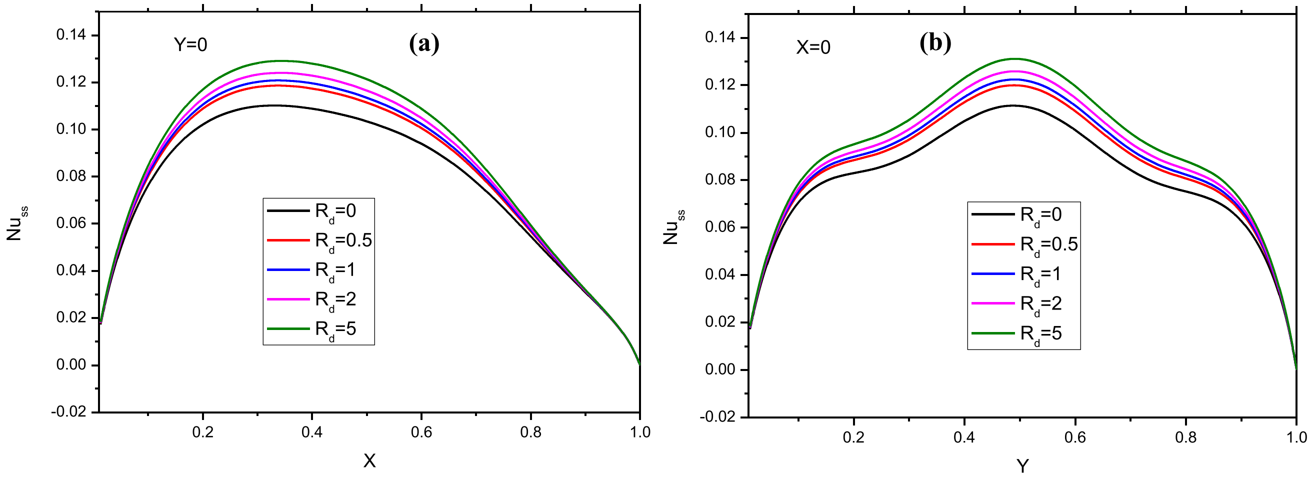

Fig. 10 Radiation heat transfer parameter profiles of the local Nusselt number of solid phase along the bottom (left figure) and the left side (right figure) for TiO_2–Cu/water Hybrid Nanofluid at $Ha=10$, $Q=1$, $Da=10^{-3}$, $Ri=1$, $Gr_c=1$, $H^*=10$, $\varepsilon=0.5$, $\gamma=0.5$, $\Phi=\pi/3$, $\lambda=$, $\alpha=$, $\phi_{Cu}=\phi_{TiO2}=\phi/2$, $\phi=0.05$

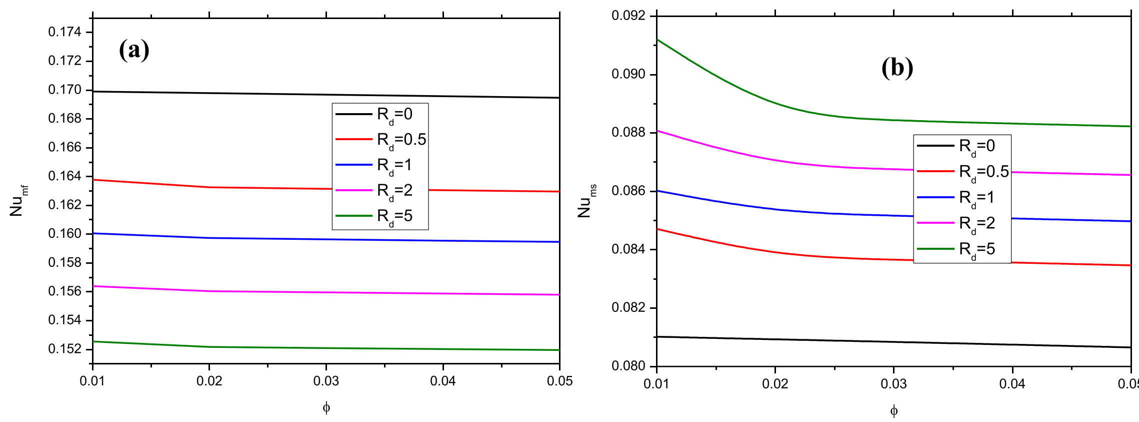

Fig. 11 Radiation heat transfer parameter profiles of the average Nusselt number of fluid phase (a) and solid phase (b) for TiO_2–Cu/water nanofluid at $Ha=10$, $Q=1$, $Da=10^{-3}$, $Ri=1$, $Gr_c=1$, $H^*=10$, $\varepsilon=0.5$, $\gamma=0.5$, $\Phi=\pi/3$, $\lambda=$, $\alpha=$, $\phi_{Cu}=\phi_{TiO2}=\phi/2$, $\phi=0.05$

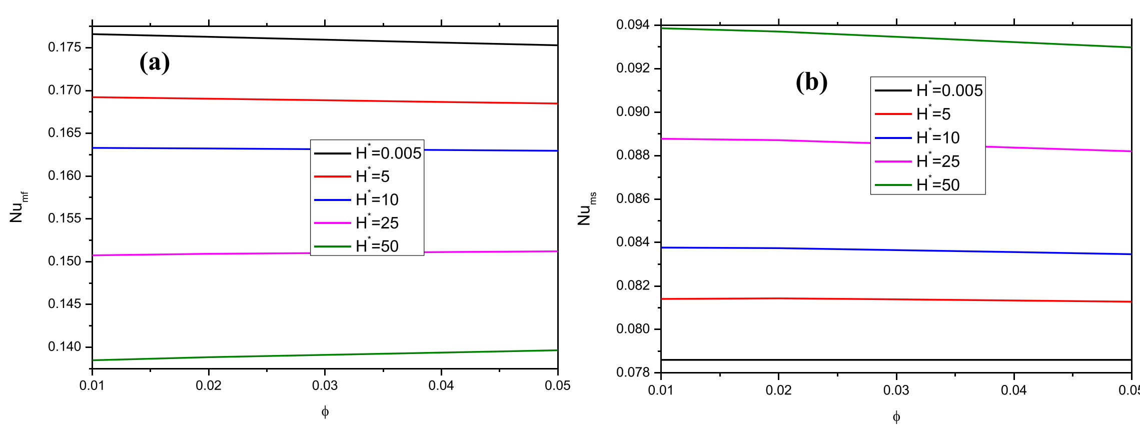

Fig. 12 Internal heat transfer parameter profiles of the average Nusselt number of fluid phase (left) and solid phase (right) for TiO_2–Cu/water nanofluid at $Ha=10$, $Q=1$, $Da=10^{-3}$, $Ri=1$, $Gr_c=1$, $R_d=0.5$, $\varepsilon=0.5$, $\gamma=0.5$, $\Phi=\pi/3$, $\lambda=$, $\alpha=$, $\phi_{Cu}=\phi_{TiO2}=\phi/2$, $\phi=0.05$

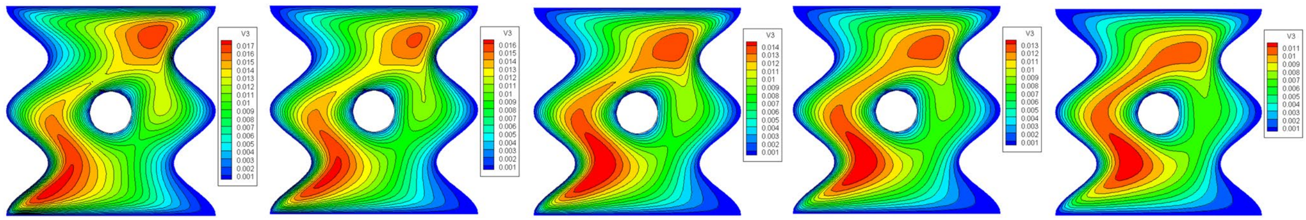

Fig. 13 Effect of the porosity (ε = {0.4, 0.5, 0.6, 0.7, 0.9}from left to right) the isotherms of fluid phase for TiO_2–Cu/water nanofluid at the moderate values; $Ha = 10$, $Q = 1$, $Da = 10^{-3}$, $Ri = 1$, $Gr_c = 1$, $H.^* = 10$, $R_d = 0.5$, $\gamma = 0.5$, $\Phi = \pi/3$, $\lambda =$, $\alpha =$, $\phi_{Cu} = \phi_{\ TiO2} = \phi/2$, $\phi = 0.05$

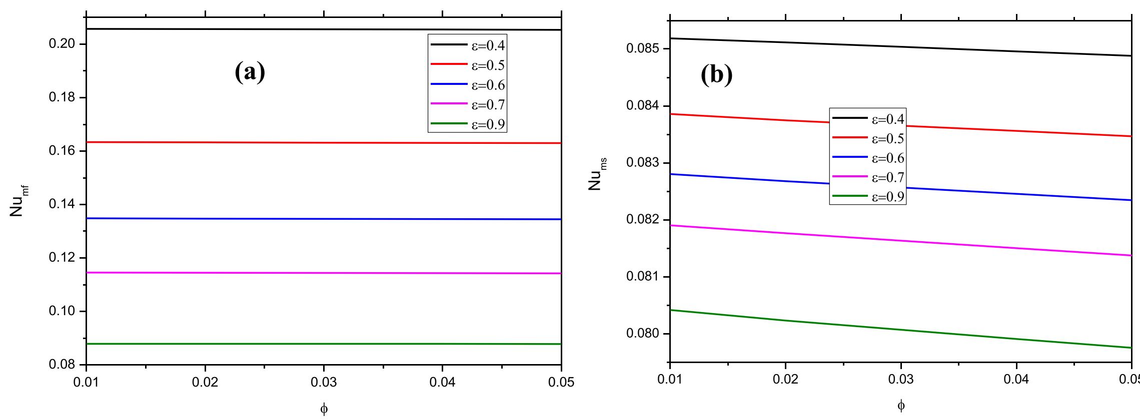

Fig. 14 Porosity parameter profiles of the average Nusselt number of fluid phase (left) and solid phase (right) for TiO_2–Cu/water Hybrid Nanofluid at $Ha = 10$, $Q = 1$, $Da = 10^{-3}$, $Ri = 1$, $Gr_c = 1$, $H^* = 10$, $R_d = 0.5$, $\gamma = 0.5$, $\Phi = \pi/3$, $\lambda =$, $\alpha =$, $\phi_{Cu} = \phi_{\ TiO2} = \phi/2$, $\phi = 0.05$

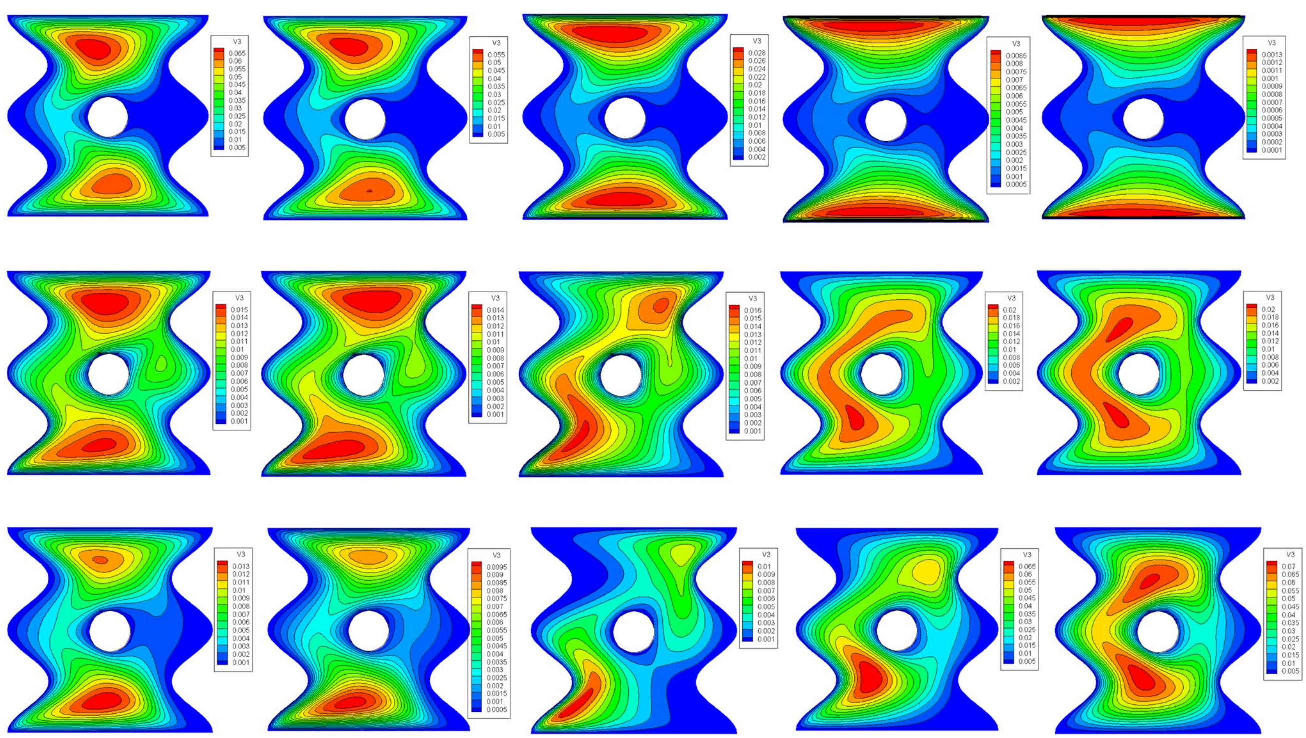

Fig.15 Effect of Darcy number variation (Da = {10^{-1}, 10^{-2}, 10^{-3}, 10^{-4}, 10^{-5}}from left to right) on contours of streamlines (1st row), isotherms of fluid phase (2nd row), isoconcentrations (3rd row), for TiO_2–Cu/water hybrid nanofluid at the moderate values; $Ha = 10$, $Q = 1$, $Ri = 1$, $Gr_c = 1$, $H^* = 10$, $R_d = 0.5$, $\varepsilon = 0.5$, $\gamma = 0.5$, $\Phi = \pi/3$, $\lambda =$, $\alpha =$, $\phi_{Cu} = \phi_{\ TiO2} = \phi/2$, $\phi = 0.05$

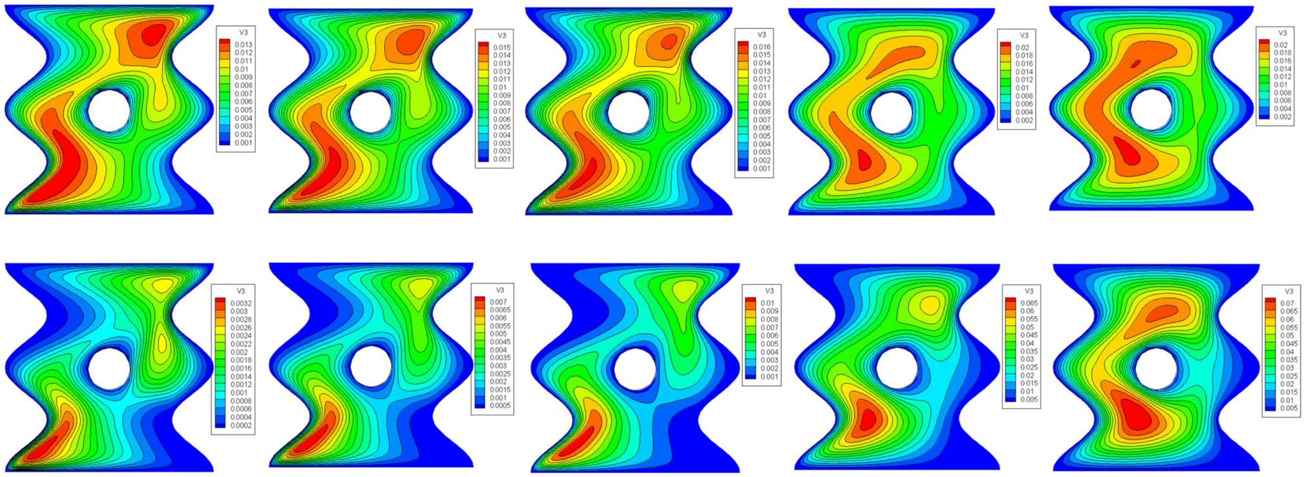

Fig. 16 Effect of Richardson number variation (Ri = {0.5,0.8,1,10,100} on contours of streamlines (1st row), and isotherms of fluid phase (2nd row), for TiO_2–Cu/water hybrid nanofluid at the moderate values; $Ha=10$, $Q=1$, $H^*=10$, $R_d=0.5$, $\varepsilon=0.5$, $\gamma=0.5$, $\Phi=\pi/3$, $\lambda=$, $\alpha=\pi/3$, $\phi_{Cu}=\phi_{TiO2}=\phi/2, \phi=0.05$

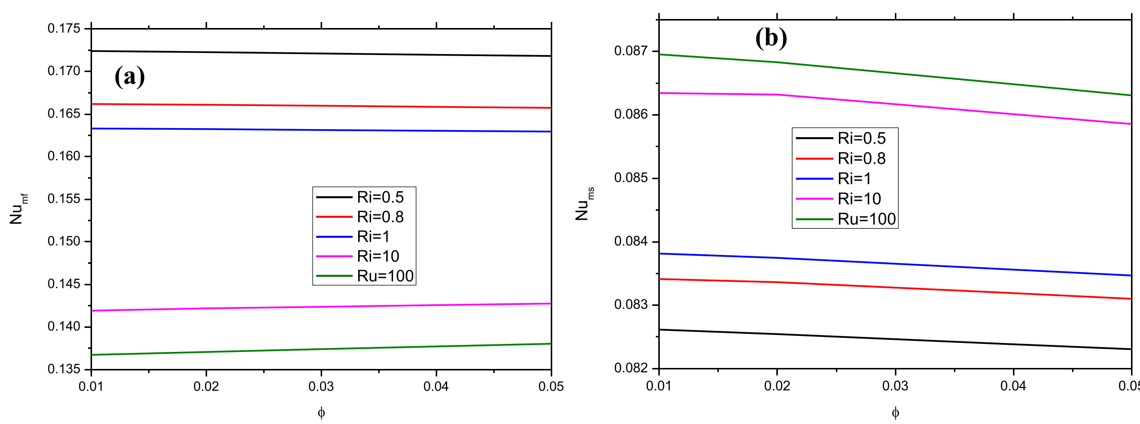

Fig. 17 Richardson number profiles of the average Nusselt number of fluid phase (left) and solid phase (right) for TiO_2–Cu/water Hybrid Nanofluid at $Ha=10$, $Q=1$, $Da=10^{-3}$, $Gr_c=1$, $H^*=10$, $R_d=0.5$, $\varepsilon=0.5$, $\gamma=0.5$, $\Phi=\pi/3$, $\lambda=$, $\alpha=$, $\phi_{Cu}=\phi_{TiO2}=\phi/2$, $\phi=0.05$

The effect of Hartmann number appears as a feedback of the inclination angle of the magnetic field used in the model as it is shown at Fig. 8 for the streamlines. Consequently, the magnetic field enhances the contours deformation along the second diagonal of the square cavity. Accordingly, as "*Ha*" increases, the supreme isotherms extend through the left side of the cavity (because of the cavity inclination angle effect too) and join to each other. Therefore, the magnetic field supports the thermal equilibrium case where the fluid and solid isotherms are congruent. Iso-concentrations contours show a slightly reasonable response to the isotherm's dynamics may be because both of them is added to momentum conservation equations as a linear component. Fluid Nusselt number along the bottom boundary (Fig. 9) shows variations at the left side of the cavity as "*Ha*" changes. By the way, the difference between left and right halves is discussed above (Fig. 6). The noticeable point here is that Hartmann number suppresses the heat transfer (more than ~ 18%); meaning that the magnetic field has a negative effect on the forced convection which clearly appears at Fig. 9 for the average fluid Nusselt number. Therefore, the magnetic field works for the equilibrium between the forced and natural convection regimes.

Solid Nusselt number (Fig. 10) along the bottom shows a somewhat change near to the midpoint as the radiation parameter increases while it keeps as a latent at the limits. The fluid average Nusselt number (Fig. 11) discovers the inhibitory role of the radiation which could be due to the Titanium nanoparticles characters while for the solid mean

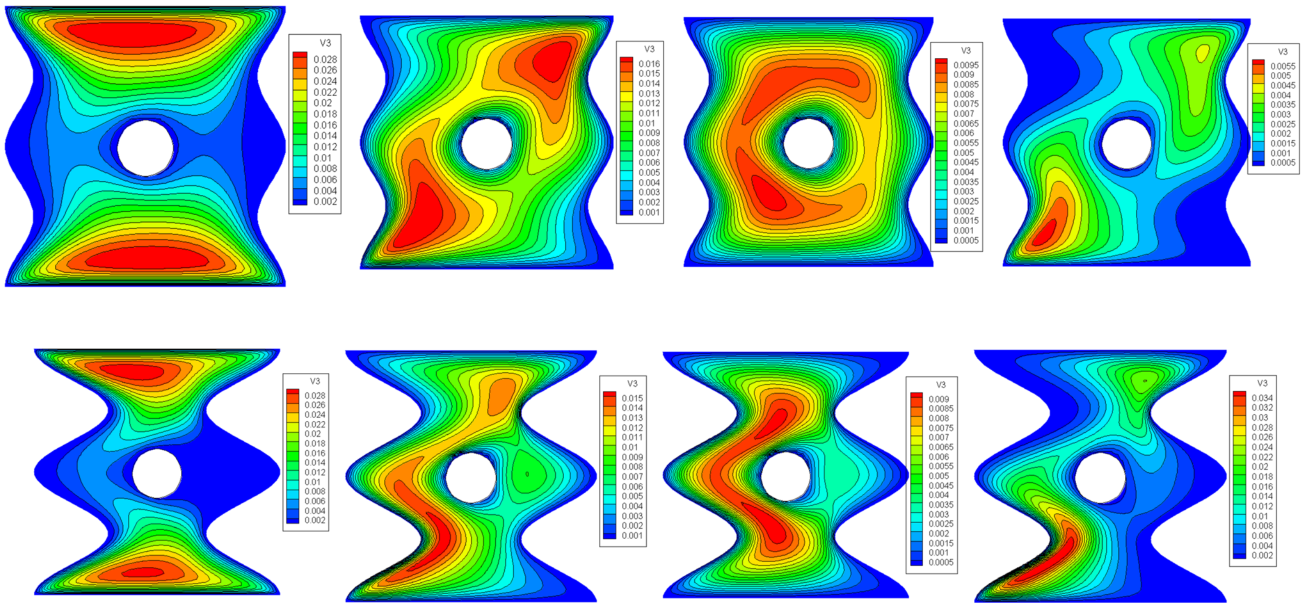

Fig. 18 Effect of wave amplitude variation (1st row: A = 0.05, 2nd row: A = 0.15) on the streamline, isotherms of fluid phase, isotherms of solid phase, isoconcentration (from left to right respectively) for TiO_2–Cu/water hybrid nanofluid at the moderate values; $Ha = 10$, $Q = 1$, $Da = 10^{-3}$, $Ri = 1$, $Gr_c = 1$, $H^* = 10$, $R_d = 0.5$, $\varepsilon = 0.5$, $\gamma = 0.5$, $\Phi = \pi/3$, $\lambda =$, $\alpha =$, $\phi_{Cu} = \phi_{TiO2} = \phi/2$, $\phi = 0.05$

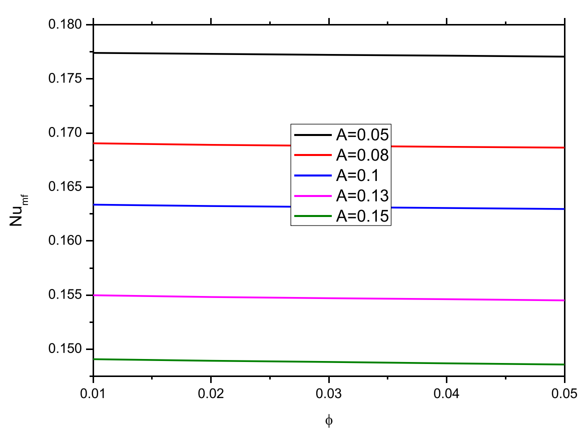

Fig. 19 Wave amplitude parameter profiles of the fluid average Nusselt number for TiO_2–Cu/water hybrid nanofluid at $Ha = 10$, $Q = 1$, $Da = 10^{-3}$, $Ri = 1$, $Gr_c = 1$, $H^* = 10$, $R_d = 0.5$, $\varepsilon = 0.5$, $\gamma = 0.5$, $\Phi = \pi/3$, $\lambda =$, $\alpha =$, $\phi_{Cu} = \phi_{TiO2} = \phi/2$, $\phi = 0.05$

Nusselt number is vice versa. As we can see, the fluid Nusselt number decreases about 10% while the solid Nusselt number increases about ~ 13%. Figure 12 reflects again the opposite behavior of heat transfer at the solid and fluid phases. It's found that the solid average Nusselt number is enhanced by "H^*" while it decays for the fluid phase. The reason could be referred to some factors such as the thermophysical properties of the used nanoparticles, the dominant convection regime, or the boundary condition effects.

Streamlines increase as the porosity increases (Fig. 13) which agrees with the natural behavior. On the other hand, Fig. 14 shows that the average Nusselt number decreases as the porosity increases, because of the forced convection decay. Exhaustively, the average fluid Nusselt falls down ~ 60% while the average solid Nusselt descends only ~ 6%. In the same context, Fig. 15 shows the Darcy number effect, where "*Da*" tracks the permeability at the unit area intersection. Decreasing "*Da*" means weak forced convection which clearly appears from streamlines. Consequently, the supreme isotherms vortices transfer from the top/bottom boundaries to the circular source at the center. The amazing phenomenon is that the concentration descends all over the boundaries while grows up around the circle heat source.

It's known that the augmentation for the Richardson number supports the natural convection [76], therefore the streamlines and isotherms are concentrated around the heat source (Fig. 16). As a consequence the fluid Nusselt number is depressed ~ 23% while the solid Nusselt number arises ~ 7% (Fig. 17). Th interpretation is for the large "*Ri*", the natural convection dominates the fluid flow regime, so the fluid temperature difference between the heat source and the other sides decreases in general, but for solid temperature difference is still great due to the non-thermal equilibrium condition. Ultimately, for the cavity geometry, Fig. 18 shows the effect of wave amplitude. As shown, for small *A*, the contours present uniform vortices as the fluid mass increases. As "*A*" increases, the average fluid Nusselt number (Fig. 19) decreases ~ 15% because as "A" increases, the fluid flow is hampered. Therefore, the convection regime is deficient and fluid Nusselt number descends.

5 Conclusion

The mixed convection phenomenon of hybrid nanofluids within an undulating porous cavity has been investigated within this paper. The contours of the streamlines, isotherms of both fluid and solid phases and isoconcentrations have been inspected as well as the profiles of local and average Nusselt number of the fluid/solid phase under local thermal non-equilibrium case at various key parameters such as the coefficient of heat generation/absorption Q, Hartmann number Ha, porosity parameter ε, an inter-phase heat transfer coefficient H^{*}, undulation parameter λ, Darcy parameter Da, magnetic field inclination angle Φ, and hybrid nanofluid parameter ϕ. The remarkable points at the thermodynamic model under the study could be concluded as:

- The hybrid nanofluid around the circular heat source is somewhat clotted where there is low temperature and very slow motion,
- This infers that the isolated wavy sides put down the buoyancy force which is the main pillar of natural convection,
- The local thermal non-equilibrium case (LTNE) plays a prominent role as it could create some isolated regions through the entire cavity domain. Therefore, the fluid isotherms are pulled toward the movable surfaces while the solid isotherms concentrated close to the central heat source,
- Consequently, the heat transfer is not accompanied with the mass transfer. Moreover, there is somewhat an isolation between the nanofluid mass and the solid matrix,
- The driven lids mounting at top and bottom surfaces enforces the forced convection dominancy,
- In this arrangement, the circular heat source serves as a thermal barrier and flow resistance.
- The fluid response to heat generation "Q" is much stronger (~ 100%) than the solid response,
- The magnetic field strengthens the thermal equilibrium state which satisfies the balance between the natural convection and the forced convection,
- The thermal effect of the parameters {Ha, R_d, H*, Ri} is reverse when the phase changes (solid/fluid). While the effect of {Q, ε} doesn't change. This because the last two factors don't change the convection regime. However, the former parameters are either directly related to the LTNE case or change the dominant regime obviously.
- The average fluid Nusselt number descent due to the porosity is ~ 60% which represents ten times the of that at the solid descent.
- Iso-concentrations contours show a slightly reasonable response to the isotherm's dynamics when the magnetic field varies.
- The magnetic field has a negative effect on the forced convection.
- The average Nusselt number decreases as the porosity increases.

Acknowledgements Authors appreciate the great efforts provided by Prof. Sameh E. Ahmed. His help has greatly improved the article status.

Author contributions Prof. Mansour has established the theoretical basis of the model and has conducted the numerical investigation, Bakier has introduced for the study, discussed the results, and organized the sections through the paper.

Funding Open access funding provided by The Science, Technology & Innovation Funding Authority (STDF) in cooperation with The Egyptian Knowledge Bank (EKB). During the preparation of this manuscript, no funds, grants, or other support was received by the authors.

Data availability The datasets generated during and/or analysed during the current study are available from the corresponding author on reasonable request.

Declarations

Conflict of interest The authors have no relevant financial or non-financial interests to disclose.

References

1. Sheikholeslami M, Gorji-Bandpy M, Ganji DD, Rana P, Soleimani S (2014) Magnetohydrodynamic free convection of Al_2O_3–water nanofluid considering Thermophoresis and Brownian motion

effects. Comput Fluids 94:147–160. https://doi.org/10.1016/j.compfluid.2014.01.036
2. Bakar N A, Karimipour A, Roslan R (2016) Effect of magnetic field on mixed convection heat transfer in a lid-driven square cavity. J Thermodyn 2016, Article ID 3487182, 14 p. https://doi.org/10.1155/2016/3487182
3. Armaghani T, Chamkha AJ, Rashad AM, Mansour MA (2020) Inclined magneto: convection, internal heat, and entropy generation of nanofluid in an I-shaped cavity saturated with porous media. J Therm Anal Calorim 142:2273–2285. https://doi.org/10.1007/s10973-020-09449-6
4. Sadeghi MS, Tayebi T, Dogonchi AS, Nayak MK, Waqas M (2021) Analysis of thermal behavior of magnetic buoyancy-driven flow in ferrofluid—filled wavy enclosure furnished with two circular cylinders. Int Commun Heat Mass Transf 120:104951. https://doi.org/10.1016/j.icheatmasstransfer.2020.104951
5. Dogonchi AS, Tayebi T, Karimi N, Chamkha AJ, Alhumade H (2021) Thermal-natural convection and entropy production behavior of hybrid nanoliquid flow under the effects of magnetic field through a porous wavy cavity embodies three circular cylinders. J Taiwan Inst Chem Eng 124:162–173. https://doi.org/10.1016/j.jtice.2021.04.033
6. Ghadikolaei SS, Yassari M, Sadeghi H, Hosseinzadeh K, Ganji DD (2017) Investigation on thermophysical properties of TiO_2–Cu/H_2O hybrid nanofluid transport dependent on shape factor in MHD stagnation point flow. Powder Technol 322:428–438. ISSN 0032-5910. https://doi.org/10.1016/j.powtec.2017.09.006
7. Syazana N, Bachok N, Arifin N, Rosali H (2020) MHD flow past a nonlinear stretching/shrinking sheet in carbon nanotubes: stability analysis. Chin J Phys 65:436–446. ISSN 0577-9073. https://doi.org/10.1016/j.cjph.2020.03.003
8. Reddy PBA, Reddy NB, Suneetha S (2013) Radiation effects on MHD flow past an exponentially accelerated isothermal vertical plate with uniform mass diffusion in the presence of heat source. J Appl Fluid Mech 5(3):119–126. https://doi.org/10.36884/jafm.5.03.19454
9. Rashidi M M, Bagheri S, Momoniat E, Freidoonimehr N (2017) Entropy analysis of convective MHD flow of third grade non-Newtonian fluid over a stretching sheet. Ain Shams Eng J 8(1):77–85. ISSN 2090-4479. https://doi.org/10.1016/j.asej.2015.08.012
10. Jakeer S, Polu BAR (2022) Homotopy perturbation method solution of magneto-polymer nanofluid containing gyrotactic microorganisms over the permeable sheet with Cattaneo-Christov heat and mass flux model. Proc Inst Mech Eng Part E J Process Mech Eng 236(2):525–534. https://doi.org/10.1177/09544089211048993
11. Scott D, Anderson R, Figliola R (1988) Blockage of natural convection boundary layer flow in a multizone enclosure. Int J Heat Fluid Flow 9(2):208–214
12. Chang LC, Lloyd JR, Yang KT (1982) A finite difference study of natural convection in complex enclosures. In: 7th Int. Heat Transfer Conf., Munich, Germany
13. Eshaghi S, Izadpanah F, Dogonchi AS, Chamkha AJ, Ben Hamida MB, Alhumade H (2021) The optimum double-diffusive natural convection heat transfer in H-Shaped cavity with a baffle inside and a corrugated wall. Case Stud Therm Eng 28:101541
14. Nansteel MW, Greif R (1982) Natural convection in undivided and partially divided rectangular enclosures. J Heat Transf 104:527–532
15. Lin NN, Bejan A (1983) Natural convection in a partially divided enclosure. Int J Heat Mass Transf 26:1867–1878
16. Sahoo RK, Sarkar A, Sastri VMK (1993) Effect of an obstruction on natural convection heat transfer in vertical channels—a finite element analysis. Int J Numer Methods Heat Fluid Flow 3(3):267–276
17. Said SA, Krane RJ (1990) An analytical and experimental investigation of natural convection heat transfer in vertical channel with a single obstruction. Int J Heat Mass Transf 33:1121–1134
18. Seyyedi SM, Dogonchi AS, Hashemi-Tilehnoee M, Ganji DD, Chamkha AJ (2020) Second law analysis of magneto-natural convection in a nanofluid filled wavy-hexagonal porous enclosure. Int J Numer Methods Heat Fluid Flow 30(11):4811–4836
19. Tayebi T, Dogonchi AS, Karimi N, Ge-JiLe H, Chamkha AJ, Elmasry Y (2021) Thermo-economic and entropy generation analyses of magnetic natural convective flow in a nanofluid-filled annular enclosure fitted with fins. Sustain Energy Technol Assess 46:101274
20. Dogonchi AS, Waqas M, Afshar SR, Seyyedi SM, Hashemi-Tilehnoee M, Chamkha AJ, Ganji DD (2020) Investigation of magneto-hydrodynamic fluid squeezed between two parallel disks by considering Joule heating, thermal radiation, and adding different nanoparticles. Int J Numer Methods Heat Fluid Flow 30(2):659–680
21. Shahriari A, Ashorynejad HR, Pop I (2019) Entropy generation of MHD nanofluid inside an inclined wavy cavity by lattice Boltzmann method. J Therm Anal Calorim 135:283–303. https://doi.org/10.1007/s10973-018-7061-x
22. Sheremet MA, Oztop HF, Pop I, Al-Salem K (2016) MHD free convection in a wavy open porous tall cavity filled with nanofluids under an effect of corner heater. Int J Heat Mass Transf 103:955–964. https://doi.org/10.1016/j.ijheatmasstransfer.2016.08.006
23. Dogonchi AS, Mishra SR, Chamkh AJ, Ghodrat M, Elmasry Y, Alhumade H (2021) Thermal and entropy analyses on buoyancy-driven flow of nanofluid inside a porous enclosure with two square cylinders: finite element method. Case Stud Therm Eng 27:101298
24. Mandal DK, Biswas N, Manna NK, Gorla RSR, Chamkha AJ (2021) Role of surface undulation during mixed bioconvective nanofluid flow in porous media in presence of oxytactic bacteria and magnetic fields. Int J Mech Sci 211:106778
25. Li C, Xiao J, Zhang Y, Chen XD (2019) Mixing in a soft-elastic reactor (SER): a simulation study. Can J Chem Eng 97:676–686. https://doi.org/10.1002/cjce.23351
26. Zou J, Xiao J, Zhang Y, Li C, Chen XD (2020) Numerical simulation of the mixing process in a soft elastic reactor with bionic contractions. Chem Eng Sci 220:115623. https://doi.org/10.1016/j.ces.2020.115623
27. Shekaramiz M, Fathi S, Ataabadi H A, Kazemi-Varnamkhasti H, Toghraie D (2021) MHD nanofluid free convection inside the wavy triangular cavity considering periodic temperature boundary condition and velocity slip mechanisms. Int J Therm Sci 170: Article ID 107179
28. Rashad AM, Ismael MA, Chamkha AJ, Mansour MA (2016) MHD mixed convection of localized heat source/sink in a nanofluid-filled lid-driven square cavity with partial slip. J Taiwan Inst Chem Eng 68:173–186
29. Jakeer S, Reddy PBA, Rashad AM, Nabwey HA (2021) Impact of heated obstacle position on magneto-hybrid nanofluid flow in a lid-driven porous cavity with Cattaneo-Christov heat flux pattern. Alex Eng J 60:821–835. https://doi.org/10.1016/j.aej.2020.10.011
30. Sheikholeslami M, Sadoughi M (2017) Mesoscopic method for MHD nanofluid flow inside a porous cavity considering various shapes of nanoparticles. Int J Heat Mass Transf 113:106–114
31. Aghaei A, Khorasanizadeh H, Sheikhzadeh GA (2019) A numerical study of the effect of the magnetic field on turbulent fluid flow, heat transfer and entropy generation of hybrid nanofluid

in a trapezoidal enclosure. Eur Phys J Plus 134:310. https://doi.org/10.1140/epjp/i2019-12681-3
32. Khanafer K, Vafai K, Lightstone M (2003) Buoyancy-driven heat transfer enhancement in two-dimensional enclosure utilizing nanofluids. Int J Heat Mass Transf 46:3639–3653
33. Chamkha AJ, Selimefendigil F, Ismael MA (2016) Mixed convection in a partially layered porous cavity with an inner rotating cylinder. Numer Heat Transf Part A Appl 69(6):659–675
34. Aly AM, Raizah ZAS (2019) Mixed convection in an inclined nanofluid filled-cavity saturated with a partially layered porous medium. J Therm Sci Eng Appl 11(4):041002–041011
35. Chamkha AJ, Mansour MA, Rashad AM, Kargarsharifabad H, Armaghani T (2020) Magnetohydrodynamic mixed convection and entropy analysis of nanofluid in gamma-shaped porous cavity. J Thermophys Heat Transf 34(4):836–847
36. Tiwari R, Das M (2007) Heat transfer augmentation in a two-sided lid-driven differentially heated square cavity utilizing nanofluids. Int J Heat Mass Transf 50:2002–2018
37. Billah MM, Rahman DM, Razzak MA, Rahman S, Mekhilef S (2013) Unsteady buoyancy-driven heat transfer enhancement of nanofluids in an inclined triangular enclosure. Int Commun Heat Mass Transf 49:115–127
38. Chamkha AJ, Dogonchi AS, Ganji DD (2018) Magnetohydrodynamic nanofluid natural convection in a cavity under thermal radiation and shape factor of nanoparticles impacts: a numerical study using CVFEM. Appl Sci 8:2396. https://doi.org/10.3390/app8122396
39. Suresh S, Venkitaraj KP, Selvakumar KP, Chandrasekar M (2012) Effect of Al2O3–Cu/water hybrid nanofluid in heat transfer. Exp Therm Fluid Sci 38:54–60
40. Jeena PK, Brocchi EA, Motta MS (2001) In-situ formation of Cu–Al_2O_3 nanoscale composites by chemical routes and studies on their microstructures. Mater Sci Eng A 313:180–186
41. Biswas N, Mondal MK, Mandal DK, Manna NK, Gorla RSR, Chamkha AJ (2022) A narrative loom of hybrid nanofluid-filled wavy walled tilted porous enclosure imposing a partially active magnetic field. Int J Mech Sci 217:107028
42. Oh S-T, Lee J-S, Sekino T, Niihara K (2001) Fabrication of Cu dispersed Al_2O_3 nanocomposite using Al_2O_3/CuO and Al_2O_3/Cu nitrate mixtures. Scr Mater 44:2117–2120
43. Toghraie D, Chaharsoghi VA, Afrand M (2016) Measurement of thermal conductivity of ZnO–TiO_2/EG hybrid nanofluid. J Therm Anal Calorim 125:527–535
44. Huang D, Wu Z, Sunden B (2016) Effects of hybrid nanofluid mixture in plate heat exchangers. Exp Therm Fluid Sci 72:190–196
45. Han ZH, Yang B, Kim SH, Zachariah MR (2007) Application of hybrid sphere/carbon nanotube particles in naonofluids. Nanotechnology 18:105701
46. Afshar SR, Mishra SR, Dogonchi AS, Karimi N, Chamkha AJ, Abulkhair H (2021) Dissection of entropy production for the free convection of NEPCMs-filled porous wavy enclosure subject to volumetric heat source/sink. J Taiwan Inst Chem Eng 128:98–113
47. Labib MN, Nine MdJ, Afrianto H, Chung H, Jeong H (2013) Numerical investigation on effect of base fluids and hybrid nanofluid in forced convective heat transfer Int. J Therm Sci 71:163–171
48. Arefmanesh A, Najafi M, Nikfar M (2010) MLPG application of nanofluid flow mixed convection heat transfer in a wavy wall cavity. Comput Model Eng Sci 69(2):91–118. https://doi.org/10.3970/cmes.2010.069.091
49. Alsabery AI, Ismael MA, Chamkha AJ, Hashim I (2020) Impact of finite wavy wall thickness on entropy generation and natural convection of nanofluid in cavity partially filled with non-Darcy porous layer. Neural Comput Appl 32:13679–13699
50. Das PK, Mahmud S (2003) Numerical investigation of natural convection inside a wavy enclosure. Int J Therm Sci 42:397–406
51. Kumar BR (2000) A study of free convection induced by a vertical wavy surface with heat flux in a porous enclosure. Numer Heat Transf Part A Appl 37:493–510
52. Alsabery AI, Tayebi T, Chamkha AJ, Hashim I (2020) Natural convection of Al_2O_3–water nanofluid in a non-Darcian wavy porous cavity under the local thermal non-equilibrium condition. Sci Rep 10:18048. https://doi.org/10.1038/s41598-020-75095-5
53. Baytaş AC (2003) Thermal non-equilibrium natural convection in a square enclosure filled with a heat-generating solid phase, non-Darcy porous medium. Int J Energy Res 27:975–988
54. Sheremet MA, Pop I, Nazar R (2015) Natural convection in a square cavity filled with a porous medium saturated with a nanofluid using the thermal nonequilibrium model with a Tiwari and Das nanofluid model. Int J Mech Sci 100:312–321
55. Zargartalebi H, Ghalambaz M, Sheremet MA, Pop I (2017) Unsteady free convection in a square porous cavity saturated with nanofluid: the case of local thermal nonequilibrium and Buongiorno's mathematical models. J Porous Media 20(11):999–1016. https://doi.org/10.1615/JPorMedia.v20.i11.50
56. Tahmasebi A, Mahdavi M, Ghalambaz M (2018) Local thermal nonequilibrium conjugate natural convection heat transfer of nanofluids in a cavity partially filled with porous media using Buongiorno's model. Numer Heat Transf Part A Appl 73:254–276
57. Nield DA, Kuznetsov AV, Xiong M (2002) Effect of local thermal non-equilibrium on thermally developing forced convection in a porous medium. Int J Heat Mass Transf 45:4949–4955
58. Kim SJ, Jang SP (2002) Effects of the Darcy number, the Prandtl number, and the Reynolds number on local thermal non-equilibrium. Int J Heat Mass Transf 45:3885–3896
59. Amiri A, Vafai K, Kuzay TM (1995) Effects of boundary conditions on non-Darcian heat transfer through porous media and experimental comparisons. Numer Heat Transf Part A 27:651–664
60. Mahmoudi Y, Karimi N (2014) Numerical investigation of heat transfer enhancement in a pipe partially filled with a porous material under local thermal non-equilibrium condition. Int J Heat Mass Transf 68:161–173
61. Izadi M, Mehryan SAM, Sheremet MA (2018) Natural convection of CuO–water micropolar nanofluids inside a porous enclosure using local thermal non-equilibrium condition. J Taiwan Inst Chem Eng 88:89–103
62. Sivasankaran S, Alsabery AI, Hashim I (2018) Internal heat generation effect on transient natural convection in a nanofluid-saturated local thermal non-equilibrium porous inclined cavity. Physica A 509:275–293
63. Tahmasebi A, Mahdavi M, Ghalambaz M (2018) Local thermal nonequilibrium conjugate natural convection heat transfer of nanofluids in a cavity partially filled with porous media using Buongiorno's model. Numer Heat Transf Part A 73(4):254–276. https://doi.org/10.1080/10407782.2017.1422632
64. Cho C-C (2018) Heat transfer and entropy generation of mixed convection flow in Cu-water nanofluid-filled lid-driven cavity with wavy surface. Int J Heat Mass Transf 119:163–174. https://doi.org/10.1016/j.ijheatmasstransfer.2017.11.090
65. Hussain S, Oztop HF, Mehmood K, Abu-Hamdeh N (2018) Effects of inclined magnetic field on mixed convection in a nanofluid filled double lid-driven cavity with volumetric heat generation or absorption using finite element method. Chin J Phys 56:484–501. https://doi.org/10.1016/j.cjph.2018.02.002
66. Madkhali HA, Nawaz M, Saif RS, Afzaal MF, Alharbi SO, Alaoui MK (2021) Comparative analysis on the roles of different nanoparticles on mixed convection heat transfer in Newtonian fluid in Darcy-Forchheimer porous space subjected to convectively heated boundary. Int Commun Heat Mass Transf 128:105580
67. Maxwell JA (1904) Treatise on electricity and magnetism, 2nd edn. Oxford University Press, Cambridge

68. Brinkman HC (1952) The viscosity of concentrated suspensions and solution. J Chem Phys 20:571–581
69. Aminossadati SM, Ghasemi B (2009) Natural convection cooling of a localised heat source at the bottom of a nanofluid-filled enclosure. Eur J Mech B/Fluids 28:630–640
70. Yang L, Hu Y (2017) Toward TiO_2 nanofluids—part 1: preparation and properties. Nanoscale Res Lett 12:417. https://doi.org/10.1186/s11671-017-2184-8
71. Li W, Zou C, Li X (2018) Thermo-physical properties of cooling water-based nanofluids containing TiO_2 nanoparticles modified by Ag elementary substance for crystallizer cooling system. Powder Technol 329:434–444. ISSN 0032-5910. https://www.sciencedirect.com/science/article/pii/S0032591018301116
72. Ahmed SE (2016) Mixed convection in thermally anisotropic non-Darcy porous medium in double lid-driven cavity using Bejan's heatlines. Alex Eng J 55(1):299–309. ISSN 1110-0168. https://doi.org/10.1016/j.aej.2015.07.016
73. Ahmed SE, Mansour MA, Rashad AM (2020) MHD natural convection from two heating modes in fined triangular enclosures filled with porous media using nanofluids. J Therm Anal Calorim 139:3133–3149. https://doi.org/10.1007/s10973-019-08675-x
74. Cheong HT, Sivasankaran S, Bhuvaneswari M (2017) Natural convection in a wavy porous cavity with sinusoidal heating and internal heat generation. Int J Numer Methods Heat Fluid Flow 27:287
75. Khanafer KM, Chamkha AJ (1999) Mixed convection flow in a lid-driven enclosure filled with a fluid saturated porous medium. Int J Heat Mass Transf 42:2465–2481
76. Mandal DK, Biswas N, Manna NK, Gayen DK, Gorla RSR, Chamkha AJ (2022) Thermo-fluidic transport process in a novel M-shaped cavity packed with non-Darcian porous medium and hybrid nanofluid: Application of artificial neural network (ANN). Phys Fluids 34:033608. https://doi.org/10.1063/5.0082942